

Detection and localisation of the highly active FRB 20240114A with MeerKAT

J. Tian¹*, K. M. Rajwade², I. Pastor-Marazuela¹, B. W. Stappers¹, M. C. Bezuidenhout^{3,4}, M. Caleb^{5,6}, F. Jankowski⁷, E. D. Barr⁸, M. Kramer⁸

¹Jodrell Bank Centre for Astrophysics, Department of Physics and Astronomy, The University of Manchester, Manchester M13 9PL, UK

²Astrophysics, The University of Oxford, Denys Wilkinson Building, Keble Road, Oxford OX1 3RH, UK

³Centre for Space Research, North-West University, Potchefstroom 2531, South Africa

⁴Department of Mathematical Sciences, University of South Africa, Cnr Christiaan de Wet Rd and Pioneer Avenue, Florida Park, 1709, Roodepoort, South Africa

⁵Sydney Institute for Astronomy, School of Physics, The University of Sydney, NSW 2006, Australia

⁶ARC Centre of Excellence for Gravitational Wave Discovery (OzGrav), Hawthorn, 3122, Victoria, Australia

⁷LPC2E, Université d'Orléans, CNRS, 3A Avenue de la Recherche Scientifique, F-45071 Orléans, France

⁸Max-Planck-Institut für Radioastronomie, 53121 Bonn, Germany

Accepted XXX. Received YYY; in original form ZZZ

ABSTRACT

We report observations of the highly active FRB 20240114A with MeerKAT using the Ultra-High Frequency (UHF; 544–1088 MHz) and L-band (856–1712 MHz) receivers. A total of 62 bursts were detected in coherent tied-array beams using the MeerTRAP real-time transient detection pipeline. We measure a structure-optimising dispersion measure of $527.65 \pm 0.01 \text{ pc cm}^{-3}$ using the brightest burst in the sample. We find the bursts of FRB 20240114A are generally detected in part of the broad band of MeerKAT, $\sim 40\%$ in the UHF and $\sim 30\%$ in the L-band, indicating the band limited nature. We analyse the fluence distribution of the 44 bursts detected at UHF, constraining the fluence completeness limit to $\sim 1 \text{ Jy ms}$, above which the cumulative burst rate follows a power law $R(> F) \propto (F/1 \text{ Jy ms})^\gamma$ with $\gamma = -1.8 \pm 0.2$. Using channelised telescope data captured in our transient buffer we localise FRB 20240114A in the image domain to RA = 21h27m39.86s, Dec = +04d19m45.01s with an uncertainty of 1.4 arcsec. This localisation allows us to confidently identify the host galaxy of FRB 20240114A. Also using the transient buffer data we perform a polarimetric study and demonstrate that most of the bursts have $\sim 100\%$ linear polarisation fractions and up to $\sim 20\%$ circular polarisation fractions. Finally, we predict the flux density of a potential persistent radio source (PRS) associated with FRB 20240114A is $\simeq [0.6\text{--}60] \mu\text{Jy}$ based on the simple relation between the luminosity of the PRS and the rotation measure arising from the FRB local environment.

Key words: techniques: interferometric - methods: data analysis - methods: observational - fast radio bursts.

1 INTRODUCTION

Fast radio bursts (FRBs) are bright ($\sim 10 \text{ mJy}$ – 100 Jy ; e.g. Petroff et al. 2016; Shannon et al. 2018), short-duration (μs – ms ; e.g. Cho et al. 2020; Nimmo et al. 2021) bursts of radio emission with extragalactic origins, mainly hosted by star-forming galaxies (Gordon et al. 2023). The last few years have witnessed a rapid expansion of the FRB population, with most discovered by the Canadian Hydrogen Intensity Mapping Experiment (CHIME; CHIME Collaboration et al. 2022) Fast Radio Burst project (CHIME/FRB; CHIME/FRB Collaboration et al. 2018). However, the physical ori-

gin of FRBs remains unknown although several lines of evidence favor a neutron star origin (e.g. Zhang 2023).

While most FRBs appear to be one-off events, a subset (~ 50 known) are observed to repeat (CHIME/FRB Collaboration et al. 2023), allowing detailed studies of these FRB sources with targeted follow-up observations. Collecting a large sample of bursts from a repeating FRB source can reveal important features in the burst properties and progress our understanding of the burst emission mechanism and the influence of propagation effects, such as the downward drifting of subpulses in frequency with time (Hessels et al. 2019; CHIME/FRB Collaboration et al. 2019a; Caleb et al. 2020; Pleunis et al. 2021) and the evolution of polarisation position angles with time (Michilli et al. 2018; Luo et al. 2020; Nimmo et al. 2021). In particular, measuring the polarisation fractions and

* E-mail: jun.tian@manchester.ac.uk

rotation measures (RMs) of a large sample of bursts could reveal any depolarisation towards lower frequencies and RM scattering, which are intriguing features of repeating FRBs that have started to emerge recently and shed light on the complexity of magnetized environments associated with repeating FRBs (Feng et al. 2022b; Anna-Thomas et al. 2023).

Repeating FRBs also allow for periodicity searches. On long timescales (\sim days), there is evidence for periodic activity from FRB 20121102A (Rajwade et al. 2020; Cruces et al. 2021) and FRB 20180916B (CHIME/FRB Collaboration et al. 2020a), which might reflect an orbital (Ioka & Zhang 2020), rotational (Beniamini et al. 2020) or precession (Levin et al. 2020) period. On short timescales (\sim 1 ms – 1 s), quasi-periodic substructures have been reported for FRB 20200120E (Majid et al. 2021), FRB 20191221A (CHIME/FRB Collaboration et al. 2022) and FRB 20201020A (Pastor-Marazuela et al. 2023). Such substructures resemble the quasi-periodic micropulses seen in some radio pulsars (Mitra et al. 2015; De et al. 2016) and magnetars (Kramer et al. 2024), favoring a neutron star origin for FRBs. These motivate further searches for periodicities in repeating FRBs, especially in the range of \sim 1 s – 1000 s, which could indicate associations with magnetars.

Apart from studies of the emission properties of repeating FRBs, their repeating nature facilitates accurate localisation of the source. The first subarcsecond localisation of an FRB was made through targeted observations of FRB 20121102A, associating this repeater with a low-metallicity star-forming dwarf galaxy (Chatterjee et al. 2017; Tendulkar et al. 2017). Later, more subarcsecond localisations of repeating FRBs revealed a wide range of host galaxies, including a massive spiral galaxy (Marcote et al. 2020), a star-forming, dusty and massive galaxy similar to that of apparent non-repeaters (Ravi et al. 2022), a globular cluster (Kirsten et al. 2022), and an additional dwarf galaxy (Niu et al. 2022). Such a diversity of host galaxies imply that multiple progenitors may be responsible for the FRB phenomenon, motivating the characterisation of a larger sample, which could provide further insight into the origin of FRB repetition (Gordon et al. 2023).

FRB 20240114A is a repeating source recently discovered by CHIME/FRB at a dispersion measure (DM) of 527.7 pc cm^{-3} and reported to be in an active state from the end of January 2024 (Shin & CHIME/FRB Collaboration 2024). It was shown to be highly energetic with the brightest burst reaching a fluence of $919 \pm 97 \text{ Jy ms}$. An initial localisation of the source by CHIME/FRB gave RA = 21:27:39.89, Dec = +04:21:00.36 with a \sim 30 arcsec uncertainty. These motivated us to propose for Director’s Discretionary Time to follow up with MeerKAT (proposal id: DDT-20240206-JT-01), which was allocated 2 hr of observation on 2024 February 9. Subsequent detections of many more bursts by Murriyang (Uttarkar et al. 2024), the Five-hundred-meter Aperture Spherical radio Telescope (FAST; Zhang et al. 2024a) and the upgraded Giant Metrewave Radio Telescope (uGMRT; Kumar et al. 2024; Panda et al. 2024) confirmed the hyperactivity of FRB 20240114A. Our observation with MeerKAT improved the source position to \sim arcsec precision and made the first identification of the host galaxy (Tian et al. 2024), which were then used by uGMRT and FAST in their targeted searches, leading to the detections of hundreds of bursts (Panda et al. 2024; Zhang et al. 2024b). Later, the European Very Long Baseline Interferometry (VLBI) PRECISE team localised FRB 20240114A to RA = 21:27:39.835, Dec = +04:19:45.634 with an uncertainty of 200 milliarcseconds (Snelders et al. 2024), which is consistent with our localisation.

In this paper we describe the detection of 62 bursts from FRB 20240114A with MeerKAT and present the burst properties

and localisation of the source. In Section 2, we describe the observational configuration of MeerKAT and the transient detection pipeline. Our results are then presented in Section 3. We discuss the host galaxy of FRB 20240114A and inferred properties in Section 4, followed by conclusions in Section 5.

2 OBSERVATIONS AND DATA

The MeerKAT observations of FRB 20240114A were carried out on 2024 February 09 as part of the DDT proposal DDT-20240206-JT-01 with the Ultra-High Frequency (UHF; 544–1088 MHz) and L-band (856–1712 MHz) receivers on 40 of the 64 13.5-m dishes in the inner \sim 1-km core of the array. The observations lasted 2 hr with 1 hr at UHF and 1 hr at L-band. The primary beam full width at half-maximum (FWHM) at the UHF and L-band are \sim 3.2 deg² and \sim 1.3 deg², respectively (Mauch et al. 2020). At that time, FRB 20240114A was localised to a \sim 30 arcsec region by CHIME/FRB, well within the primary beam of MeerKAT. Therefore, we recorded imaging data for the FRB source localisation as well as beamformed data to search for repeat bursts.

Thanks to the Transient User Supplied Equipment (TUSE), a real-time transient detection backend instrument developed by the Meer(more) TRAnsients and Pulsars (MeerTRAP; Sanidas et al. 2018; Bezuidenhout et al. 2022; Rajwade et al. 2022; Caleb et al. 2023; Jankowski et al. 2023; Driessen et al. 2024) project, we are able to trigger voltage buffer dumps while searching for bursts in real-time. Our follow-up of FRB 20240114A started with the coherent beamforming mode, where voltages from the inner 40 dishes were coherently combined and phased using the Filterbank and Beamforming User Supplied Equipment (FBFUSE), a many-beam beamformer that was designed and developed at the Max Planck Institute for Radio Astronomy in Bonn (Barr 2018; Chen et al. 2021). We formed 768 tied-array coherent beams (CBs) overlapping at 75% of the beam power that tiled out from the best localisation of FRB 20240114A reported by CHIME/FRB up to a radius of \sim 3 arcmin. Data from these CBs were arranged and ingested by the TUSE real-time single pulse search pipeline, enabling us to instantaneously detect multiple pulses from FRB 20240114A and providing a quicker initial investigation. In the case of a detection, channelised, high time resolution transient buffer data were saved for offline correlation and imaging (for the MeerTRAP voltage buffer dump system see Rajwade et al. 2024). Note that the triggering system is limited by the processing speed of the real-time pulse search and also bursts within 10 s of each other are not triggered to limit the load on the system so we did not get voltage capture triggers for all bursts.

Given the above observing strategy, our observation of FRB 20240114A resulted in two datasets: detected time-frequency data in the filterbank format from all CB detections and voltage data for all triggers. Each filterbank file contains a dispersed pulse and additional padding of 0.5 s at the start and end of the file. The full bandwidth is split into 1024 channels, corresponding to a frequency and time resolution of 0.53 MHz/481.88 μ s and 0.84 MHz/306.24 μ s at UHF and L-band, respectively. For the subset of the detections that triggered the transient buffer, we additionally recorded \sim 300 ms channelised voltage data, which had been incoherently dedispersed at the detection DM. These voltage data are Nyquist sampled across 4096 channels from \sim 60 out of 64 dishes available at that time.

2.1 Burst detection

We performed a real-time burst search on each CB targeted at FRB 20240114A using the state-of-the-art GPU-based single pulse search pipeline `ASTROACCELERATE`¹ (Armour et al. 2012; Adámek & Armour 2020). All candidates with signal-to-noise (S/N) above 8 were saved to disc in the filterbank format. See Caleb et al. 2022, Rajwade et al. 2022 and Jankowski et al. 2023 for more details on removing radio frequency interference (RFI) and sifting the candidates. After visually inspecting the pulse profiles and dynamic spectra of the candidates and removing any repetitions of the same burst detected in multiple CBs, we obtained a list of 62 bursts with detection DMs ranging from 527.84 pc cm⁻³ to 534.36 pc cm⁻³, 44 in the UHF and 18 in the L-band over the full exposure time of 2 hr. The gallery of the detected bursts dedispersed to 527.65 pc cm⁻³ (see Section 3.1) is shown in Figure 1, with their times of arrival (TOAs, barycentric and referenced to infinite frequency), detected S/Ns, burst widths and fluences being listed in Table 1. We cover ± 100 ms around the time of the burst.

2.2 Voltage data

We triggered on 48 of the 62 detected bursts, including 31 at UHF and 17 at L-band (see Table 1), and downloaded the voltage data along with the gain solutions for all available frequency channels. In order to localise the FRB source, we correlated the voltage data to create visibilities after applying the gain solutions. Images were made with `WSCLEAN` (Offringa et al. 2014; Offringa & Smirnov 2017) around the time of the burst detection with an integration time of 0.96 ms and 0.61 ms at UHF and L-band, respectively. Any bright \sim ms bursts can be identified as transient sources in these images. Note that we did not perform flux density calibration for the images, but that does not affect our localisation of the FRB source. Further details on the imaging methods can be found in Rajwade et al. 2024.

After determining the FRB position through imaging (see below), we coherently beamformed the voltage data at the best FRB coordinates to create a high time-resolution, full polarization time-frequency data product for each burst. We used the `DSPSR` package (van Straten & Bailes 2011) to write these beamformed data into an archive format that can be processed using tools from `PSRCHIVE` (Hotan et al. 2004), including `PAZI` for removing RFIs and `PAM` for transforming to Stokes parameters. Compared to the real-time data products, these archive data have a much higher resolution in time and frequency (0.13 MHz/7.5 μ s and 0.21 MHz/4.8 μ s at UHF and L-band, respectively) and full Stokes information. In addition, as we can beamform right at the interferometric localisation of FRB 20240114A using the 64 antennas (see Section 3.2), and perform coherent dedispersion with `DSPSR`, we expect the pulse signals to be much stronger in these archive data than detected in the filterbank data. All these facilitate studying the dynamic pulse structure of the bursts with voltage buffer dumps and their polarisation properties. See Rajwade et al. 2024 for more details on the beamforming process.

3 RESULTS

3.1 DM estimation

Upon detection of the FRB 20240114A bursts, we estimated the DMs that maximised the peak S/Ns of individual pulses. However, these S/N maximising DMs could result in loss of intrinsic temporal sub-structure, especially for those bursts with complex morphology and multiple components. We therefore used a structure optimising approach to measure the DM of FRB 20240114A. We selected the two brightest bursts in our sample, U29 detected in the UHF with a S/N of 177.08 and showing a simple pulse and L3 detected in the L-band with a S/N of 77.02 and showing two sub-components (see Figure 1), and ran `DM_PHASE`² (Seymour et al. 2019), a DM optimisation algorithm that maximises the coherent power across the bandwidth. We dedispersed the two bursts over a trial DM range of 520–535 pc cm⁻³ in steps of 0.01 pc cm⁻³, and obtained a structure optimising DM of 527.65 ± 0.01 pc cm⁻³ and 527.92 ± 0.14 pc cm⁻³ for the two bursts, respectively. The uncertainty on each DM was calculated through transforming the standard deviation of the coherent power spectrum into a standard deviation in DM. Given that these two DM values agree within a 2σ error, we adopt $DM = 527.65 \pm 0.01$ pc cm⁻³ for FRB 20240114A throughout this work. This DM is also consistent with that reported by CHIME/FRB.

For comparison, we computed both the S/N and structure optimising DMs for all the bursts. The distribution is shown in Figure 2. Note that we do not provide structure optimising DMs for the bursts with a low S/N (≤ 13), as this approach does not produce a good fit of the S/N–DM curve. As can be seen, most of the bursts show a DM in the range of 528–530 pc cm⁻³, which is consistent with our observation of many under-dedispersed bursts in Figure 1. This DM discrepancy corresponds to a dispersion delay of ~ 10 ms across the emission bandwidth, comparable to the pulse width of the bursts. Therefore, we do not expect significant distortion in the burst structure due to the DM variation observed here. Also, the bursts we detected from FRB 20240114A do not show narrow components and many of them have a single component, so the structure optimising algorithm does not work well on them. Additionally, the observed difference in DM is likely to be an intrinsic property of the bursts, since the DM is not expected to evolve on a timescale of a few minutes. In summary, we conclude that the DM measured from the brightest burst can be applied to all the bursts of FRB 20240114A analysed here.

3.2 Imaging and localisation

We selected the two brightest bursts detected in the L-band, L2 and L3, for imaging and localisation of the FRB 20240114A source. Note that in the L-band we can achieve a better localisation accuracy than in the UHF given the higher frequencies and thus higher resolution. For each burst, we created two images, "on" and "off", with the voltage data covering the same duration of and before the burst respectively, as shown in Figure 3. We adopted a pixel scale of 1 arcsec and size of 8192 \times 8192 pixels, and used the `WSCLEAN` algorithm (Offringa et al. 2014; Offringa & Smirnov 2017) for deconvolution. This imaging exercise also provides a check on the data quality. We identified a transient source in the on-burst image for both bursts, as indicated by the cyan circle in Figure 3. Given this source appears only at the time of the FRB detection and at

¹ <https://github.com/AstroAccelerateOrg/astro-accelerate>

² https://github.com/danielemichilli/DM_phase

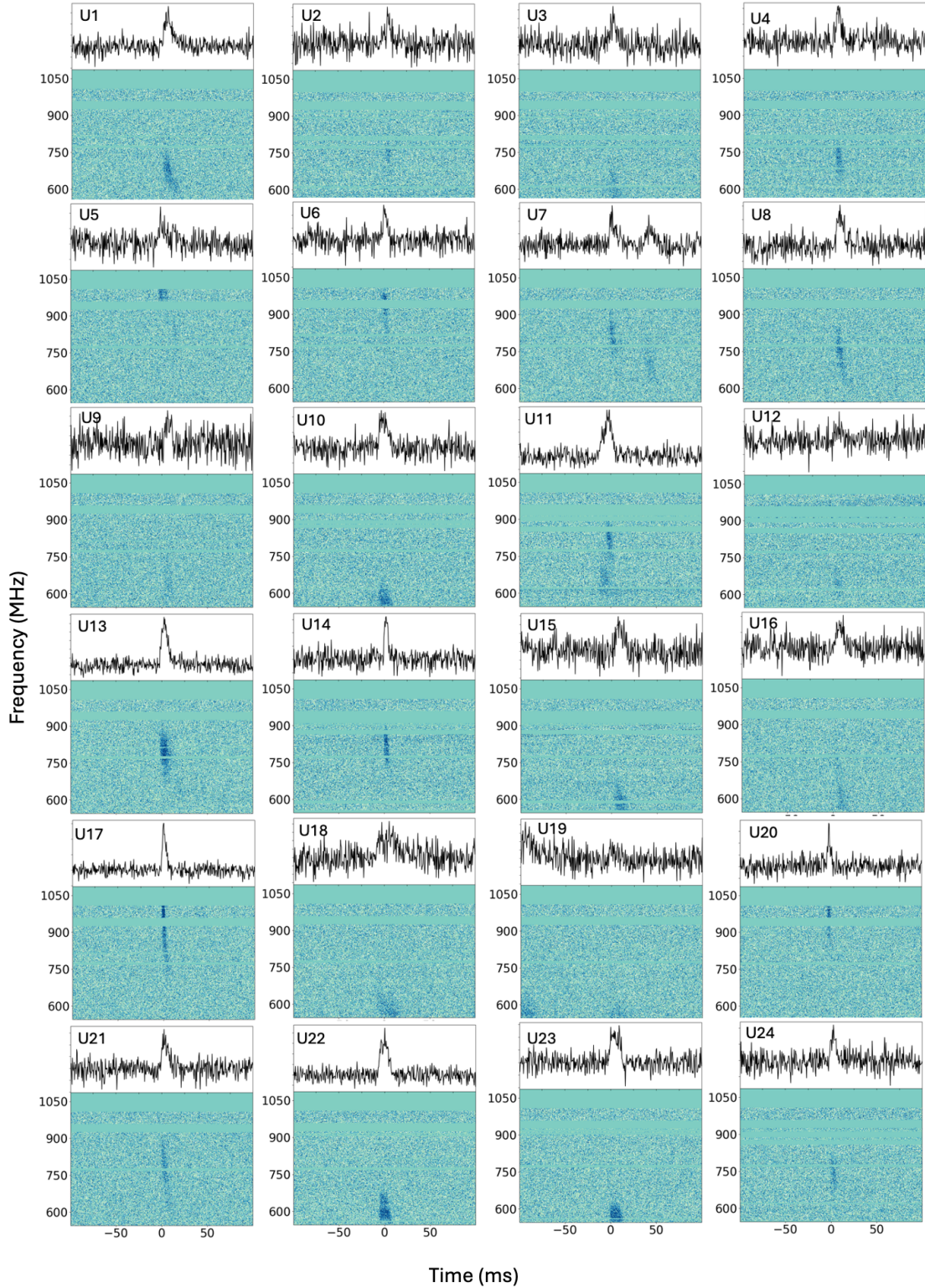


Figure 1. Dynamic spectra of the bursts detected from FRB 20240114A in chronological order. Each panel shows the dynamic spectrum of a burst from Table 1 from the filterbank data dedispersed to $527.65 \text{ pc cm}^{-3}$, the structure optimising DM determined for FRB 20240114A in Section 3.1, with the top sub-panel showing the frequency-averaged pulse profile in arbitrary units. The dynamic spectra have been binned $4\times$ in frequency. A label is given to each burst in the top-left corner with "U" and "L" indicating detection in the UHF and L-band, respectively. Burst U19 follows U18 closely, and part of the U18 emission is visible in the panel of U19. Bursts U43 and U44 were detected only ~ 50 ms apart and are presented in the same panel. So are bursts L9 and L10. The horizontal lines that show the same colour are either missing channels or flagged due to RFI.

Burst ^a	TOA ^b (MJD)	S/N _{det} ^c	Burst width ^d (ms)	Fluence ^e (Jy ms)	Error ^e (Jy ms)	Trigger ^f	L/I ^g	V /I ^g
U1	60349.25540534	22.0	8.8	2.44	0.26	Y	0.98(13)	0.16(6)
U2	60349.25567773	8.8	5.6	1.87	0.20	N		
U3	60349.25568583	11.1	8.8	3.68	0.31	N		
U4	60349.25576426	12.9	5.6	2.28	0.24	Y	0.99(15)	0.16(7)
U5	60349.25687076	12.8	11.0	2.90	0.12	Y	0.94(18)	0.18(10)
U6	60349.25922901	16.1	4.5	1.12	0.09	Y	0.79(17)	0.11(8)
U7	60349.25963037	18.4	5.6	1.60	0.18	Y	1.26(50)	0.20(22)
U8	60349.25978003	21.0	5.6	1.20	0.09	Y	1.08(16)	0.22(8)
U9	60349.25978165	8.9	7.0	0.63	0.11	N		
U10	60349.26020843	16.4	8.8	3.64	0.30	Y	0.88(17)	0.11(6)
U11	60349.26112171	30.2	8.8	2.61	0.26	Y	0.80(9)	0.41(6)
U12*	60349.26118684	6.7	1.8	0.12	0.05	N		
U13	60349.26584730	37.1	8.8	2.20	0.10	Y	1.05(10)	0.17(5)
U14	60349.26916507	20.9	3.6	2.25	0.15	Y	0.92(14)	0.22(8)
U15	60349.26918248	14.2	8.8	3.73	0.37	N		
U16	60349.27099313	12.8	7.0	1.65	0.23	Y	0.94(27)	0.23(14)
U17	60349.27108290	34.2	2.9	1.79	0.08	N		
U18	60349.27132540	13.9	21.4	2.18	0.15	Y	1.37(47)	0.35(22)
U19*	60349.27132653	6.2	8.4	0.38	0.06	N		
U20	60349.27320722	14.2	2.9	3.07	0.34	Y	1.04(17)	0.09(8)
U21	60349.27355901	20.5	5.6	0.90	0.09	Y	1.10(18)	0.16(8)
U22	60349.27609791	27.5	8.8	4.01	0.22	Y	0.91(8)	0.26(4)
U23	60349.27617901	21.3	11.0	3.34	0.20	N		
U24	60349.27657166	12.4	5.6	2.17	0.25	Y	0.99(25)	0.20(11)
U25	60349.27695634	25.4	11.0	4.88	0.34	Y	0.92(8)	0.13(4)
U26	60349.27724616	17.7	7.0	1.56	0.13	Y	0.44(8)	0.20(5)
U27	60349.27784935	12.8	5.6	1.70	0.28	Y	1.06(18)	0.07(8)
U28	60349.28100674	20.2	8.8	1.15	0.10	Y	0.98(16)	0.24(8)
U29	60349.28342559	177.2	3.6	7.00	0.10	Y	1.09(10)	0.05(4)
U30	60349.28552309	32.8	8.8	3.24	0.19	Y	0.92(8)	0.07(4)
U31	60349.28608044	28.1	5.6	2.04	0.13	Y	0.90(11)	0.30(6)
U32	60349.28708962	9.3	5.6	0.80	0.12	N		
U33	60349.28869337	23.8	4.5	1.36	0.08	Y	0.83(10)	0.14(5)
U34	60349.28901404	21.8	5.6	1.45	0.14	Y	0.99(16)	0.20(7)
U35	60349.28921046	16.6	5.6	1.74	0.12	Y	1.06(18)	0.13(9)
U36	60349.28967727	22.6	5.6	2.10	0.14	Y	0.86(9)	0.06(4)
U37	60349.29169012	87.2	7.0	7.02	0.30	Y	0.83(5)	0.12(2)
U38	60349.29212284	12.6	4.5	3.03	0.12	Y	1.33(45)	0.33(22)
U39	60349.29216244	51.8	4.5	2.11	0.11	N		
U40	60349.29217031	10.1	8.8	0.80	0.21	N		
U41	60349.29371123	16.9	5.6	1.02	0.10	Y	0.97(12)	0.30(7)
U42	60349.29569083	11.3	5.6	2.31	0.29	N		
U43	60349.29591442	15.7	8.8	1.20	0.12	Y	0.93(9)	0.14(4)
U44*	60349.29591494	7.2	7.0	0.44	0.10	N		

Table 1. Properties of the repeat bursts detected from FRB 20240114A with MeerKAT.

a: Label of each burst with "U" indicating detection at UHF and "L" at L-band. The highlighted bursts (*) were not detected by the real-time search pipeline, but identified in the visual inspection of other bursts.

b: Time of arrival in Barycentric Dynamical Time referenced to infinite frequency.

c: Reported S/N by the real-time search pipeline.

d: Boxcar equivalent burst width.

e: Fluence of each burst estimated by the radiometer equation and the associated error (see Section 3.4).

f: "Y" and "N" indicate whether the burst triggered the voltage buffer dump or not (see Section 2.2).

g: Linear and circular polarisation fraction measured from the voltage data (see Section 3.6). Burst L9 did not trigger voltage data, but follows burst L10 so closely (~ 50 ms; see Figure 1) that we can measure its polarisation properties using the voltage data of L10. The same applies to burst U44, but we do not provide measurements due to its low S/N.

the same position for different bursts, and since there is no other transient source in the images, we confirm that this is the FRB source.

In order to localise the FRB source, we need to perform an astrometric correction on the MeerKAT images. We imaged the full 300 ms of voltage data for each burst. The Python Blob Detector

and Source Finder³ (PYBDSF) algorithm was used to find the positions of all sources in these images, which were then matched to the sources in the Rapid ASKAP Continuum Survey (RACS) catalogue (McConnell et al. 2020), excluding any sources that appear resolved in the MeerKAT images. This resulted in 16 matches with the sepa-

³ <https://www.astron.nl/citt/pybdsf/>

Burst	TOA (MJD)	S/N _{det}	Burst width (ms)	Fluence (Jy ms)	Error (Jy ms)	Trigger	L/I	V /I
L1	60349.36537245	27.8	4.5	1.95	0.07	Y	0.95(9)	0.17(5)
L2	60349.36600170	63.7	2.9	1.48	0.05	Y	1.02(8)	0.09(4)
L3	60349.36671720	77.0	4.5	4.21	0.07	Y	0.93(4)	0.21(2)
L4	60349.36720463	39.5	4.5	1.56	0.07	Y	1.06(10)	0.09(4)
L5	60349.36731330	23.8	3.6	1.53	0.06	Y	1.06(21)	0.12(7)
L6	60349.36930761	50.1	4.5	2.07	0.06	Y	1.09(9)	0.14(4)
L7	60349.37039322	28.5	17.0	2.32	0.07	Y	1.04(9)	0.11(4)
L8	60349.37583829	13.2	3.6	0.61	0.06	Y	0.95(17)	0.16(8)
L9	60349.38019587	25.5	4.5	1.05	0.06	N	0.97(12)	0.14(6)
L10	60349.38019691	57.6	5.6	2.96	0.07	Y	0.94(6)	0.08(3)
L11	60349.38032034	13.2	4.5	1.13	0.13	Y	0.94(24)	0.08(11)
L12	60349.38280178	16.2	5.6	1.40	0.15	Y	1.00(19)	0.20(10)
L13	60349.38816473	11.1	3.6	0.75	0.07	Y	1.14(31)	0.24(13)
L14	60349.38915758	28.7	2.3	0.80	0.05	Y	0.92(15)	0.06(6)
L15	60349.39190003	43.6	7.0	1.97	0.13	Y	1.00(5)	0.16(3)
L16	60349.39266883	14.9	3.6	1.21	0.15	Y	1.27(27)	0.20(9)
L17	60349.39467029	32.6	4.5	1.05	0.08	Y	0.96(10)	0.11(5)
L18	60349.39728630	17.1	2.3	0.83	0.12	Y	1.12(20)	0.12(9)

Table 1 (Continued.).

rations ranging from 0.5 to 2.9 arcsec. We used the matched sources to solve for a transformation matrix to shift and rotate the MeerKAT sources to match the RACS source positions⁴. After the astrometric correction, the separations between the matched sources reduced to 0.3–2.5 arcsec with a median of 1 arcsec. We then applied the transformation matrix to the \sim ms images containing burst L2 and L3. Running `PYBDSF` on these astrometry corrected images, we found the source position to be RA = 21:27:39.82, Dec = +04:19:45.93 and RA = 21:27:39.86, Dec = +04:19:45.01 for L2 and L3, respectively. The uncertainty on the RA and Dec given by `PYBDSF` is \sim 0.1 arcsec, much smaller than the absolute astrometric uncertainty from the RACS positions (1 arcsec in both RA and Dec) and the median offset of the positions after the astrometric correction (1 arcsec). We added these uncertainties in quadrature and found the total uncertainty to be 1.4 arcsec.

The two positions obtained for FRB 20240114A are consistent with each other within the uncertainty, and \sim 1.2 arcmin away from the best CHIME/FRB position (within their 3σ error region). This is consistent with the position we quoted in ATel #16446 (Tian et al. 2024) and was later confirmed through the VLBI localisation within the PRECISE project (Snelders et al. 2024). In the following analysis we use the position of the brightest burst we detected in the L-band (L3) for FRB 20240114A.

3.3 Burst morphology

The sample of repeat bursts detected from FRB 20240114A display a wide range of burst morphologies, as shown in Figure 1. Note that there is an ambiguity in distinguishing whether two components are separate bursts or belong to the same burst. In this work, we consider two bursts being independent if they are separated by \geq 50 ms (twice the widest pulse in our sample). While most of the bursts show single-peaked pulse profiles, some comprise multiple components, e.g. bursts U7, U11, U28, U41, L6 and L7. While the sub-components in U7, U28 and U41 seem to follow the downward drifting trend usually observed in repeating

FRBs (Pleunis et al. 2021), the burst U11 shows upward drifting sub-components. This morphology has previously been observed in FRB 20121102A (Platts et al. 2021) and FRB 20201124A (Kumar et al. 2022), although it is quite rare. We also observe a frequency downward drift in most of the single-peaked repeat bursts. Taking the bright burst U37 as an example, we used the 2D autocorrelation function (ACF) to estimate the linear drift rate, yielding a value of $\Delta f/\Delta t = -25.5$ MHz ms⁻¹. The uncertainty is not well constrained with the direct Gaussian fitting approach, so is not included here. Other bursts show a drift rate between ~ -0.1 and ~ -34 MHz ms⁻¹.

The observed downward drifting in the bursts of FRB 20240114A can be simply explained using radius-to-frequency mapping (Wang et al. 2019). In this model, the FRB emission is produced by charged particles in the magnetosphere of a neutron star (NS) through curvature radiation. As the charged particles move away from the NS, the curvature radius continuously increases, corresponding to a decrease in the curvature radiation frequency. Assuming several bunches of charged particles are launched simultaneously along adjacent field lines from the NS surface, our line of sight will always catch the lower-altitude (i.e., higher frequency) emission first and the higher-latitude (i.e., lower frequency) emission later, resulting in the observed downward drifting. However, occasional upward drifting could be observed in the case that the bunches are launched at different times (Wang et al. 2020). This is consistent with the observed downward drifting and occasional upward drifting in the bursts of FRB 20240114A, and might suggest curvature radiation of electron-positron pairs within the magnetosphere of a NS to be the FRB emission mechanism.

A critical distinction between repeating FRBs and apparent one-off events is their spectral extent, with repeaters being usually narrower in frequency than one-offs (Pleunis et al. 2021). Figure 4 shows the spectral extent of the repeat bursts detected from FRB 20240114A as a function of burst arrival time. Note that there is a \sim 100 min gap between the UHF and L-band observations. We used a Gaussian function to fit the spectrum of the on-pulse region of each burst and adopted the full width at 10% of the maximum as the spectral extent. We did not fit the spectra of Bursts U12, U19 and U44 due to their low S/Ns. In comparison to the full bandwidth of the UHF (544 MHz) and L-band (856 MHz), all the repeat bursts

⁴ The code for performing the astrometric correction can be found on GitHub: https://github.com/AstroLaura/MeerKAT_Source_Matching

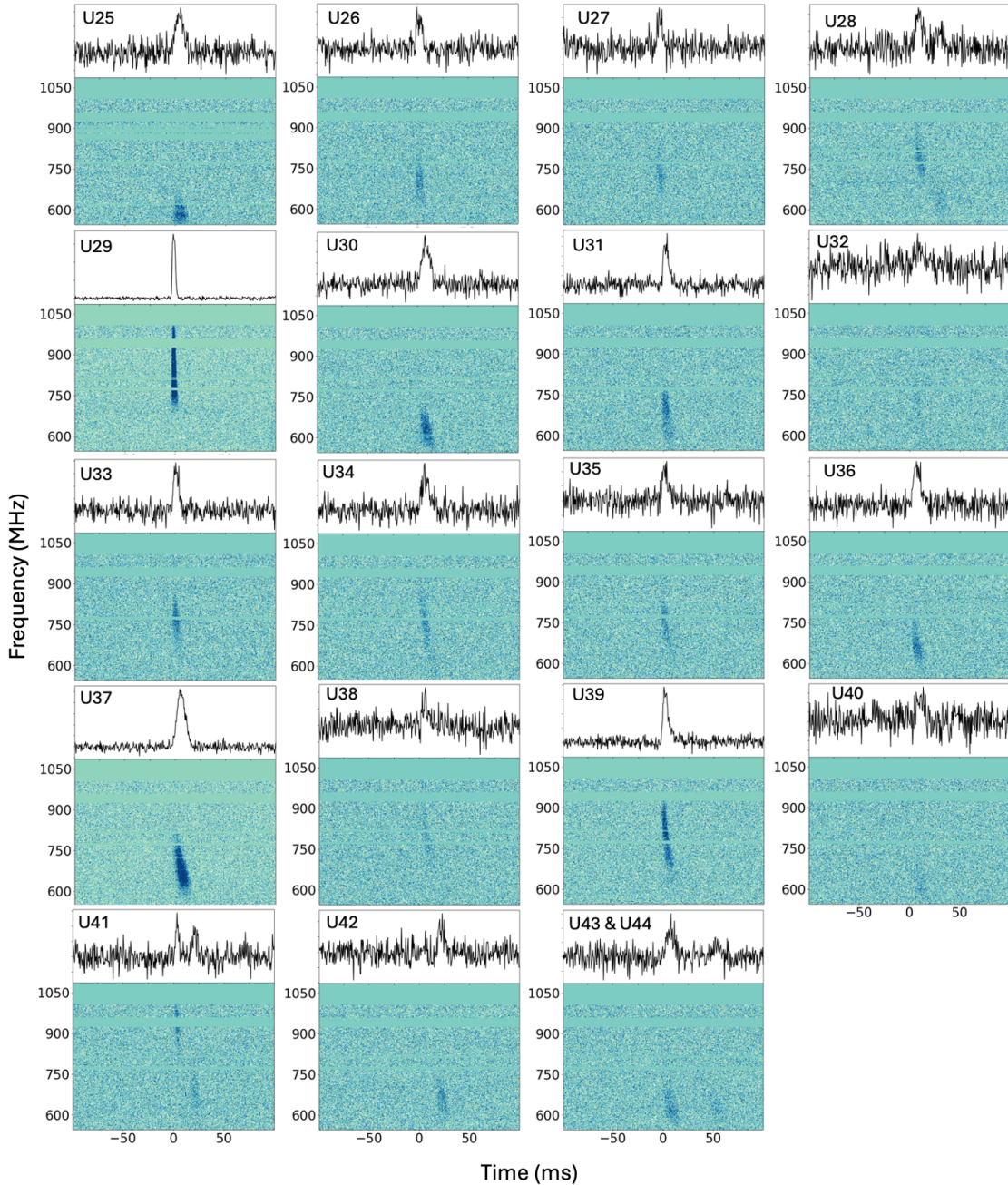


Figure 1 (Continued.).

detected from FRB 20240114A are band limited, with the average spectral occupancy being ~ 210 MHz at UHF and ~ 270 MHz at L-band, corresponding to a fractional bandwidth of $\sim 40\%$ and $\sim 30\%$, respectively. Note that the signal spectral envelope extends to the top or bottom of the bandwidth in 32 bursts (e.g. U17, U29, L1 and L3), for which our spectral extent measurements should be considered as lower limits.

Repeating FRBs are observed to display a correlation between their emission activity and frequency (Aggarwal et al. 2020). Our monitoring of the FRB 20240114A source reveals a dearth of emission above ~ 1.4 GHz, with the majority of bursts centering around ~ 700 MHz in the UHF and ~ 1 GHz in the L-band, as shown in Figure 4. It is therefore possible that the FRB emission is very faint

at higher frequencies. Further sensitive observations are needed to probe the high-frequency activity of FRB 20240114A. The preferred emission frequency of some repeating FRBs has been found to evolve on a timescale of hours to days (Gourdji et al. 2019; Pastor-Marazuela et al. 2021; Kumar et al. 2022). We do not find such a trend within our observation of FRB 20240114A.

The repeat bursts from FRB 20240114A show a wide range of burst widths from 1.84 ms to 21.4 ms, as listed in Table 1. However, the large widths of burst U18 and L7 arise from multiple distinct components being counted as a single burst. Removing these two bursts, we obtained a mean width of 5.92 ms, comparable to the burst widths of other known repeaters (Pleunis et al. 2021). Also we found the bursts in the L-band seem to be narrower than in the

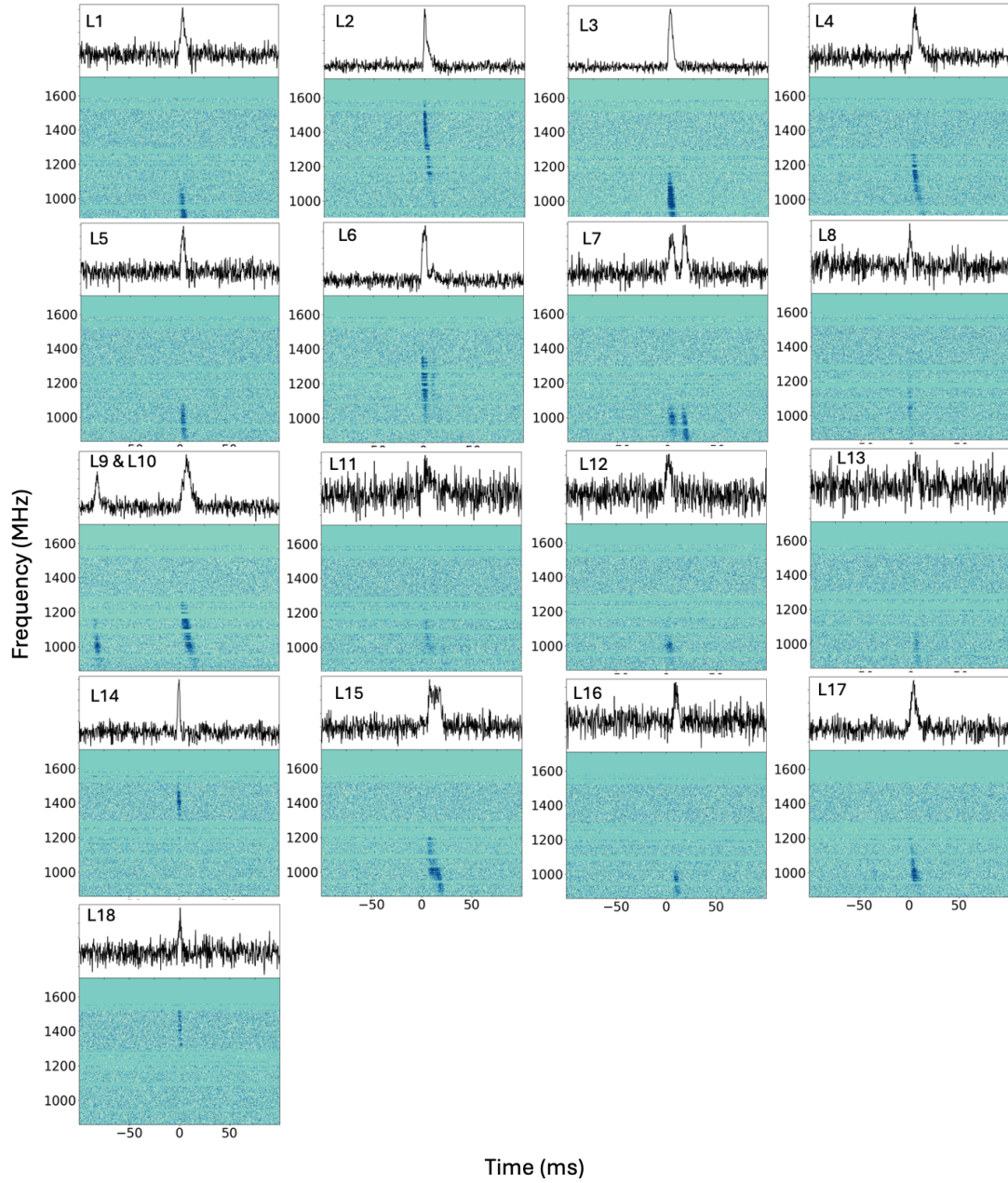


Figure 1 (Continued).

UHF, which may be caused by the intra-channel smearing, ~ 2 ms and ~ 4 ms at the center of L-band and UHF, respectively.

We do not find strong evidence in the morphology of the single-peaked repeat bursts from FRB 20240114A for temporal scattering. The scattering timescale along the line of sight of the FRB source, as predicted by the galactic distance models NE2001 and YMW16, is $0.2 \mu\text{s}$ and $0.5 \mu\text{s}$, respectively, at 1 GHz (Cordes & Lazio 2002; Yao et al. 2017; Price et al. 2021). We selected burst U29, the brightest burst in our sample and with a single-peaked narrow pulse, to constrain the scattering timescale. We performed scattering fits to this burst using a custom PYTHON-based software `SCATFIT`⁵, which convolves a single-sided exponential decay function with a Gaus-

sian base model to create a broadened pulse profile (Jankowski et al. 2023), and obtained a scattering timescale of 0.4 ± 0.2 ms at 1 GHz, much smaller than the burst width. Note that the bandwidth was split into 4 sub-bands, 3 of which have enough S/N to measure the scattering, and the scattering index was fixed to -4 . Given that scattering is difficult to model in bursts with multiple components or frequency drifting, we do not attempt to measure scattering timescales for the full sample of bursts detected from FRB 20240114A.

The dynamic spectra of several repeat bursts in our sample show scintillation, e.g. U29, U39, L3 and L6. We used the brightest burst U29 to measure the scintillation bandwidth (BW_{sc}). First we split the burst spectral extent into 7 sub-bands, from 729 MHz to 966 MHz. Then we computed the ACF of the spectral intensity for each sub-band and used a Lorentzian to fit the central peak where the half width at half maximum is the scintillation bandwidth. We

⁵ <https://github.com/fjankowsk/scatfit/>

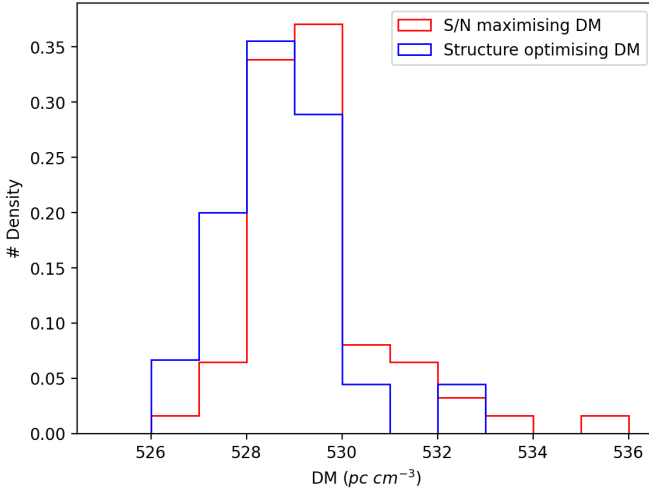


Figure 2. Distribution of S/N and structure optimising DMs for the repeat bursts detected from FRB 20240114A. This plot shows the DM variation within the sample of bursts (see Section 3.1).

obtained $BW_{sc} = 4.36 \pm 0.11$ MHz at the central frequency of 847 MHz of the burst emission, and a power-law index of $\gamma = 2.84 \pm 1.45$ for the evolution of BW_{sc} with frequency ($\propto \nu^\gamma$), which is consistent with the expected value of $\gamma = 4$ for scattering in a turbulent plasma. Along the line of sight of FRB 20240114A, the NE2001 and YMW16 galactic models predict a scintillation bandwidth of ~ 0.5 MHz at 1 GHz (Cordes & Lazio 2002; Yao et al. 2017). This suggests that the observed spectral modulation might arise from interstellar scintillation in the FRB host rather than the Milky Way. However, it is worth noting that the Galactic electron density models have large uncertainties at high Galactic latitudes (Gaensler et al. 2008), which is the case for FRB 20240114A ($b \approx -31.7$ deg). With a frequency resolution of 0.13 MHz at UHF that is comparable to the predicted decorrelation bandwidth from the Milky Way interstellar medium, we cannot rule out the models completely.

3.4 Fluences

We estimated the fluence of each burst using the modified single-pulse radiometer equation (Dewey et al. 1985) from Jankowski et al. (2023):

$$S_{\text{peak}}(S/N, W_{\text{eq}}, \vec{a}) = S/N \beta \eta_b \frac{\text{SEFD}}{\sqrt{b_{\text{eff}} N_p W_{\text{eq}}}} a_{\text{CB}}^{-1} a_{\text{IB}}^{-1}, \quad (1)$$

where S_{peak} is the peak flux density, $\vec{a} = (a_{\text{CB}}, a_{\text{IB}})$ are the attenuation factors of the detection CB and incoherent beam (IB), $\beta \approx 1$ is the digitization loss factor, $\eta_b \approx 1$ is the beamforming efficiency, SEFD is the system equivalent flux density of the MeerKAT array⁶, b_{eff} is the effective bandwidth in Hz, $N_p = 2$ is the number of polarisations, and W_{eq} is the observed equivalent boxcar pulse width in seconds. In the equation above, three parameters are frequency dependent: SEFD, a_{CB} and a_{IB} . In order to obtain the frequency-dependent SEFD, we used the polynomial models from Geyer et al.

(2021), which for the L-band is

$$\text{SEFD} = 5.71 \times 10^{-7} \nu^3 - 1.90 \times 10^{-3} \nu^2 + 1.90 \nu - 113, \quad (2)$$

and for the UHF (private communication) is:

$$\text{SEFD} = 2.30 \times 10^{-6} \nu^3 - 4.69 \times 10^{-3} \nu^2 + 2.52 \nu + 286, \quad (3)$$

where ν is the observing frequency in MHz and SEFD in Jy. Note that the above SEFD is for a single MeerKAT dish, and we need to divide that by the number of antennas used for the observation (40; see Section 2). We used the primary beam model (KATBEAM⁷) and the coherent beam model (MOSAIC⁸; Chen et al. 2021) of MeerKAT to calculate the beam correction a_{IB} and a_{CB} at the position of FRB 20240114A obtained in Section 3.2.

In order to take into account the limited spectral extents of the repeat bursts of FRB 20240114A, we split the full bandwidth into 8 sub-bands and estimated the fluence in each sub-band separately before adding them up. Specifically, we measured the S/N of the burst dedispersed to the optimal DM (see Section 3.1) in each sub-band and converted it to a flux density using Eq. 1 and fluence $F = S_{\text{peak}} W_{\text{eq}}$. Note that SEFD, a_{CB} and a_{IB} have different values in different sub-bands, and b_{eff} is the effective bandwidth of the sub-band excluding flagged channels. The final fluence of each burst summed from all the sub-bands is listed in Table 1, with the uncertainty corresponding to 1σ radiometer noise.

Figure 5 shows the cumulative distribution of the MeerKAT detected burst rate at UHF and L-band above a given fluence. There are two power-law features in the distribution, with the break being visually identified at ~ 1 Jy ms. We attribute this break to the completeness limit of MeerKAT observations and model the cumulative distribution with a function of the form $R(> F) \propto F^\gamma$. There is a detailed study of the MeerTRAP survey performance and completeness, where the fluence completeness limit is estimated to be 0.7 Jy ms (Jankowski et al. 2023), which is consistent with the value observed here. Our fit excluding bursts below the completeness limit gives a power-law index of $\gamma = -1.8 \pm 0.2$ at UHF. We do not provide fitting results for the small sample of L-band bursts. The power-law index determined here is comparable to that measured for FRB 20121102A at 1.4 GHz (-1.8 ± 0.3 ; Gourdji et al. 2019; Aggarwal et al. 2021b) and FRB20180916B at 600 MHz ($-1.3 \pm 0.3 \pm 0.1$; CHIME/FRB Collaboration et al. 2020a), but lower than the $\gamma = -1.4 \pm 0.1$ index found in Pastor-Marazuela et al. (2021) for FRB 20180916B. Note that setting a different break in fluence would affect the fitting result, e.g., a break at 2 Jy ms would give a power-law index of $\gamma = -2.6 \pm 0.2$, steeper than that with the 1 Jy ms break. In that case, it might suggest a turnover in the burst energy distribution, similar to that observed for FRB 20121102A (Li et al. 2021). A more rigorous analysis of fluence completeness is beyond the scope of this paper.

3.5 Burst rate and arrival times

We detected 44 and 18 bursts in the 1 hr MeerKAT UHF and L-band observation, respectively, with their TOAs being listed in Table 1. If all bursts above our detection limit, 0.12 Jy ms at UHF and 0.61 Jy ms at L-band (the faintest bursts detected in these two bands), have been detected, we obtain a burst rate of 44 hr^{-1} and 18 hr^{-1} at UHF and L-band, respectively. However, these estimates

⁶ See the online MeerKAT technical documentation: <https://science.ska.ac.za/meerkat>

⁷ <https://github.com/ska-sa/katbeam>

⁸ <https://github.com/wchenastro/Mosaic>

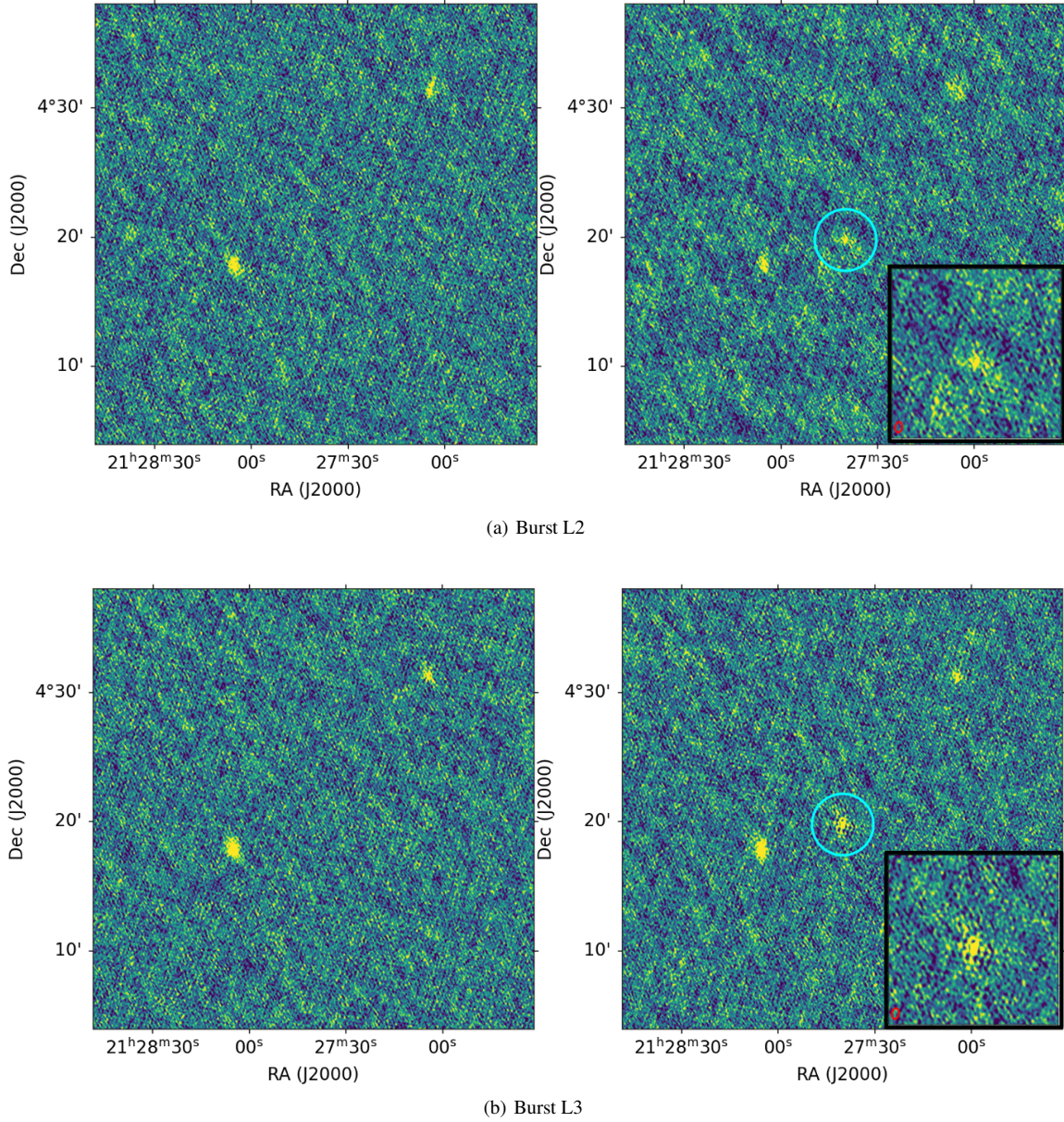


Figure 3. Images of the position of FRB 20240114A integrated over the duration of burst L2 and L3 (right) and before the burst detection (left). The cyan circle (2 arcmin radius) marks the transient source identified at the time of the FRB detection. The images have a synthesised beam size of $15 \text{ arcsec} \times 10 \text{ arcsec}$. The inset at the bottom right corner of the on-source image is a zoomed in view to display the FRB source. The red ellipse at the bottom left corner of the inset indicates the synthesised beam.

are likely to be inaccurate due to the incomplete fraction $\lesssim 1 \text{ Jy ms}$ at UHF (see Section 3.4) and the small sample at L-band. Considering only the bursts above the completeness limit of $\sim 1 \text{ Jy ms}$ at UHF, we arrive at a burst rate of $\sim 37 \text{ hr}^{-1}$. For comparison, FAST observations of FRB 20240114A between 1–1.5 GHz report an average burst rate of $\sim 20 \text{ hr}^{-1}$ above the 0.015 Jy ms fluence threshold between 2024 January 28 and February 4 (Zhang et al. 2024a) and $\sim 500 \text{ hr}^{-1}$ on 2024 March 5 (Zhang et al. 2024b), suggesting the FRB activity to be extremely variable. uGMRT observations between 550–700 MHz report a burst rate of $\sim 8 \text{ hr}^{-1}$ above a fluence of 0.6 Jy ms on 2024 February 25 (Panda et al. 2024), comparable to our measurement. All these quoted burst rates qualify FRB 20240114A as a hyperactive repeater, similar to FRB

20121102A with a peak burst rate of 122 hr^{-1} observed by FAST above 0.06 Jy ms (Li et al. 2021) and FRB 20201124A with a rate of 16 hr^{-1} by uGMRT above 7 Jy ms (Marthi et al. 2021). We also notice the FRB 20240114A source is much more active in the UHF than in the L-band, as can be seen in Figure 5. Assuming the same fluence limit for the L-band as in the UHF, we find FRB 20240114A emits $3\times$ more bursts at 816 MHz than at 1284 MHz. This frequency-dependent activity has also been observed in other repeaters, e.g. FRB 20180916B, where the FRB source emits over $10\times$ more bursts of the same fluence at 150 MHz than at 1.4 GHz (Pastor-Marazuela et al. 2021), and has been used to test the radius-to-frequency mapping model in the context of long-period magnetars (Bilous et al. 2024).

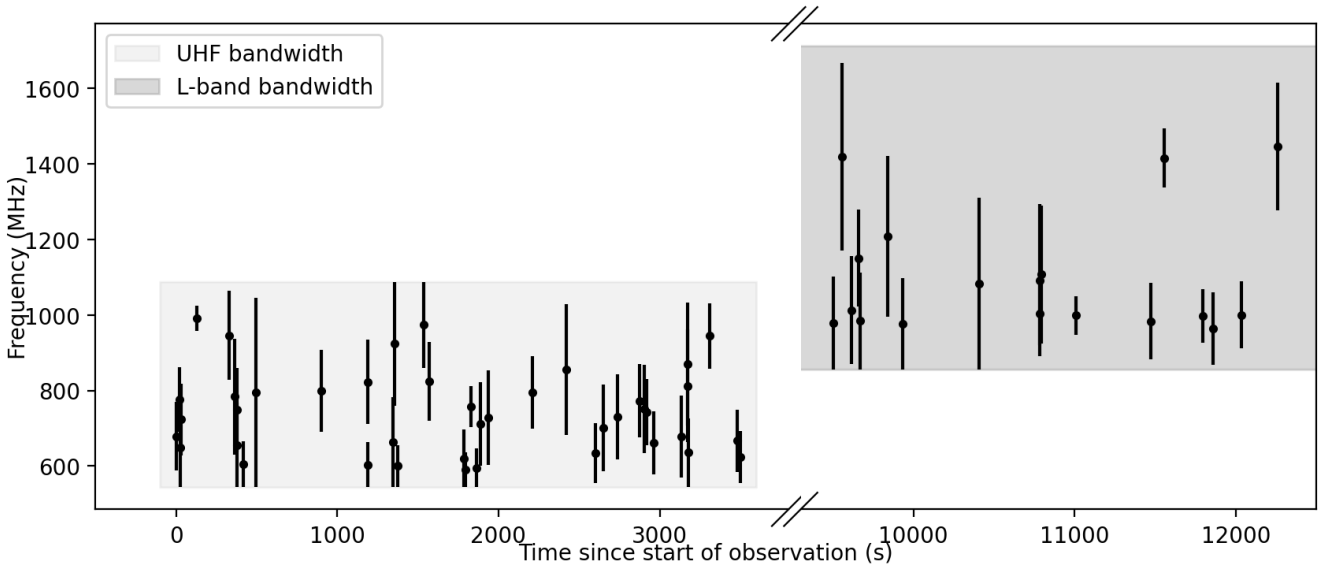


Figure 4. Burst spectral extent as a function of burst arrival time. Each point represents the central emission frequency of a burst with the error bar corresponding to the spectral extent. We did not measure the spectral extent of the three low-S/N events, U12, U19 and U44. The UHF bursts are separated from the L-band bursts by a ~ 100 min gap. The light and dark shaded regions indicate the bandwidth of the UHF and L-band observations, respectively.

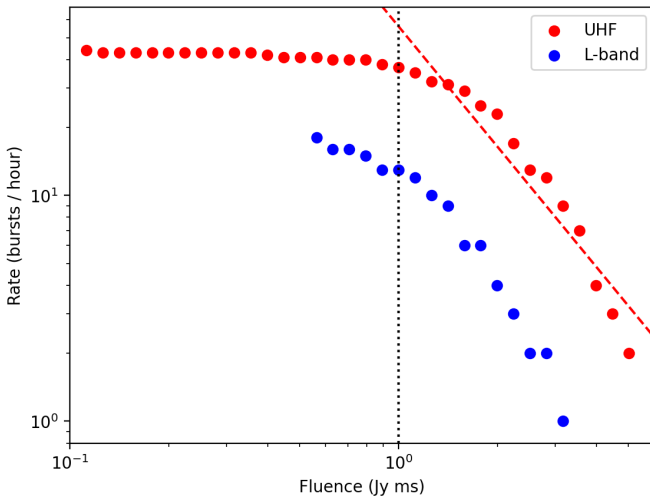


Figure 5. Cumulative burst rate function of the MeerKAT detected bursts at UHF and L-band. The vertical dotted line marks the fluence completeness limit of MeerKAT observations, and the dashed red line shows the best-fitting power law for the bursts above the completeness level at UHF. No fit is provided for the small sample of L-band bursts.

Figure 6 shows the distribution of waiting times between adjacent bursts observed in the MeerKAT UHF observation. Note that we consider two bursts being separate only if their separation is greater than 50 ms (see Section 3.3). We do not show the distribution for the L-band bursts due to their smaller sample. The mean waiting time between bursts within the 1 hr UHF observation is ~ 81 sec. If the burst occurrence follows a Poisson process, the waiting time should be exponentially distributed with a probability density function

$$f(t) = \lambda \exp(-\lambda t), \quad (4)$$

where λ is a rate parameter. With only 44 bursts, of which only 37 are above the completeness limit, we do not attempt to model the burst waiting time distribution. We limit our discussion to a comparison between the observed distribution and the Poisson distribution with a constant rate given by the mean value of the waiting times between successive bursts (see above) $\lambda \sim 1/81 \text{ s}^{-1}$, as shown in Figure 6. We found weak evidence for the observed burst waiting times being consistent with the constant-rate Poissonian repetition. This is supported by the two-sided Kolmogorov–Smirnov (KS) test that measures the maximum distance between the empirical cumulative distribution function (CDF) and the CDF corresponding to Eq. 4, which yields a p -value of ≈ 0.07 . A smaller p -value closer to zero means the two samples are more likely to arise from different distributions. Note that this result only applies to the 1 hr window of the MeerKAT observation during which FRB 20240114A is extremely active. Long-term monitoring of the FRB source may reveal any clustering behavior in the burst repetition during bursting activity, as has been demonstrated for other repeaters (e.g. [Oppermann et al. 2018](#); [Lanman et al. 2022](#)).

We also performed a periodicity search to look for any periodic pattern between the TOAs of the bursts at 1284 MHz and 816 MHz. First, the ToAs were corrected to the solar system barycentre. Then, we made use of the ALTRIS brute-force period fitting algorithm ([Morello et al. in prep](#)). ALTRIS attempts to fit the integer number of rotations within every gap between consecutive barycentred TOAs, from the shortest to the longest gap. The algorithm attempts to recursively discover the rotation counts; assuming a tentative solution for the k shortest gaps is known, a phase model is fitted to the TOA gaps, from which a range of possibilities for the rotation count $k + 1$ is calculated. If no integer rotation counts are possible, the tentative solution is discarded; otherwise, the algorithm attempts to further expand the set of new tentative solutions for the first $k + 1$ gaps. This amounts to a depth-first search of a tree of potential

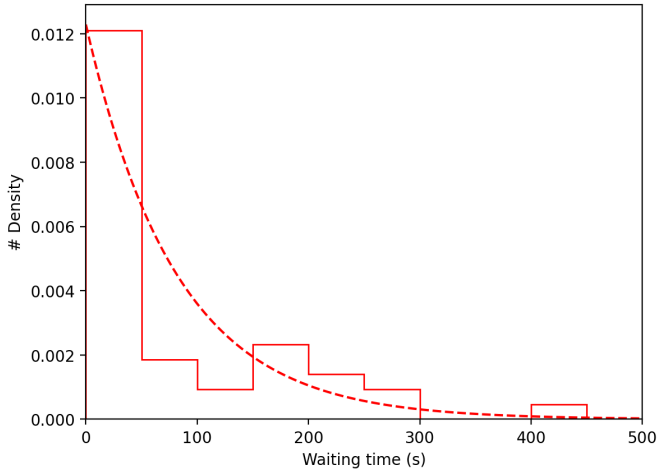


Figure 6. Distribution of the burst waiting time in the MeerKAT UHF observation. The dashed line shows the Poisson distribution with a constant rate given by the mean waiting time $\lambda \sim 1/81 \text{ s}^{-1}$.

solutions. ALTRIS did not find any solution for periods ranging from 50 ms (the smallest separation between adjacent bursts given our criterion for distinguishing separate bursts; see Section 3.3) to the total duration of the MeerKAT observations.

3.6 Polarimetry

While the bursts of FRB 20240114A were detected only in total intensity, the triggered voltage data captured complete polarisation information for some bursts (see Table 1). In order to study the polarisation properties of these bursts, we need to correct for the Faraday rotation by de-rotating the phase in Stokes Q and U produced by the RM in order to measure the polarisation fraction and polarisation position angle (PPA) as a function of time. We selected the same two bursts as in Section 3.1 and used the `RMSYNTH` tool from the software `PSRSALSA`⁹, a suite of algorithms for statistical analysis of pulsar data (Weltevrede 2016), to measure the RM of FRB 20240114A. This method transforms polarised intensity as a function of λ^2 to Faraday depth, ϕ , representing polarised intensity for different trial RMs. We searched for a range of trial RMs between $\pm 10000 \text{ rad m}^{-2}$ with a step size of 0.1 rad m^{-2} . Both bursts show a peak in the polarised intensity, corresponding to an RM of $338.1 \pm 0.1 \text{ rad m}^{-2}$ and $340.5 \pm 0.5 \text{ rad m}^{-2}$, respectively. The uncertainty on each RM was estimated by the full width at half maximum of the peak in the Faraday depth space. These results align with the preliminary analysis reported by CHIME/FRB ($\sim 325 \text{ rad m}^{-2}$; Shin & CHIME/FRB Collaboration 2024) and Parkes ($\sim 360 \text{ rad m}^{-2}$; Uttarkar et al. 2024). Similar to the exercise of a global DM for the FRB source in Section 3.1, here we adopt the RM value measured from the brightest burst in our sample, $338.1 \pm 0.1 \text{ rad m}^{-2}$, to correct the Stokes spectra of individual bursts and measure their polarisation strength.

We used `PSRSALSA` to analyse the polarisation data that had been derotated and averaged over frequency (see Section 2.2). First we removed the baseline of the Stokes parameters using `PMOD`. Then we used `PPOL` to calculate the PPA and linear polarisation intensity

$L = \sqrt{Q^2 + U^2}$. Note that the bias in L for each time sample was removed using (Wardle & Kronberg 1974)

$$L_{\text{de-bias}} = \begin{cases} L\sqrt{1 - (\frac{\sigma}{L})^2} & \text{if } L > \sigma \\ 0 & \text{otherwise,} \end{cases}$$

where $\sigma = \sqrt{(\sigma_Q^2 + \sigma_U^2)}/2$ is the off-pulse standard deviation. We set a 3σ limit on the de-biased L to obtain the significant measurements of PPA. The polarimetric pulse profiles of the 6 brightest bursts in our sample (2 at UHF and 4 at L-band), along with the significant measurements of PPA, are plotted in Figure 7. For a full presentation of the polarisation profiles see Appendix A. We measured the linear and circular polarisation fractions by averaging L/I and $|V|/I$ across the pulse profile for each burst, as shown in Table 1. Uncertainties are computed from the off-pulse standard deviation in the Stokes parameters based on the principle of error propagation. Note that we expect polarisation leakages to be small in our measurements given the FRB 20240114A source is located close to the center of the primary beam (~ 1.2 arcmin; see Section 3.2).

Figure 7 shows a diversity of PPA variations across the pulse profiles, e.g. being flat for most of the bursts, sweeping up for burst L3 and sweeping down for burst U29. This is also the case for the other bursts (see Figure A1) and reminiscent of the PPA variations observed in bursts detected from FRB 20180301A (Luo et al. 2020). Figure 8 shows the distribution of L/I and $|V|/I$ for the MeerKAT-detected repeat bursts from FRB 20240114A. We find most of the bursts have $\sim 100\%$ degree of linear polarisation and mostly up to $\sim 20\%$ degree of circular polarisation, which is consistent with the polarisation fraction measured for bursts detected from this source with FAST (Zhang et al. 2024a). Whereas highly frequency dependent depolarisation has been observed in eight repeating FRBs (Feng et al. 2022b; Mckinven et al. 2023), here we do not find such evidence in the limited sample of repeat bursts detected from FRB 20240114A as the average L/I in the UHF (0.97) and L-band (1.00) are consistent within the errors. We do not find evidence for Faraday conversion either as the average $|V|/I$ in the UHF (0.18) and L-band (0.14) are also consistent within the errors.

4 DISCUSSION

4.1 Polarisation

FRB 20240114A shows a high degree ($\sim 100\%$) of linear polarisation in all MeerKAT-detected bursts, consistent with the published sample of FRBs (Cordes & Chatterjee 2019; CHIME/FRB Collaboration et al. 2019b; Fonseca et al. 2020; Pandhi et al. 2024). The circular polarisation is low but clearly non-zero in many bursts, with a fraction up to 41% in Burst U11. This is unsurprising given the wide range of circular polarisation fractions up to $\sim 70\%$ observed in other active repeaters, e.g. FRBs 20201124A, 20121102A and 20190520B (Hilmarsson et al. 2021; Feng et al. 2022a; Jiang et al. 2022; Kumar et al. 2022; Xu et al. 2022), and suggests circular polarisation could be an essential feature of repeating FRB emission. We also found a diversity of PPA variations across the pulse profiles of FRB 20240114A, with the largest variation spanning a range of ~ 50 deg (e.g. U34, U41 and L16; see Figure A1). Such a large variation in PPA indicates a varying orientation of the magnetic field with respect to the line of sight, and resembles those seen from radio pulsars and magnetars, implying a magnetospheric origin for the FRB emission (Luo et al. 2020; Kumar et al. 2022).

⁹ <https://github.com/weltevrede/psrsalsa>

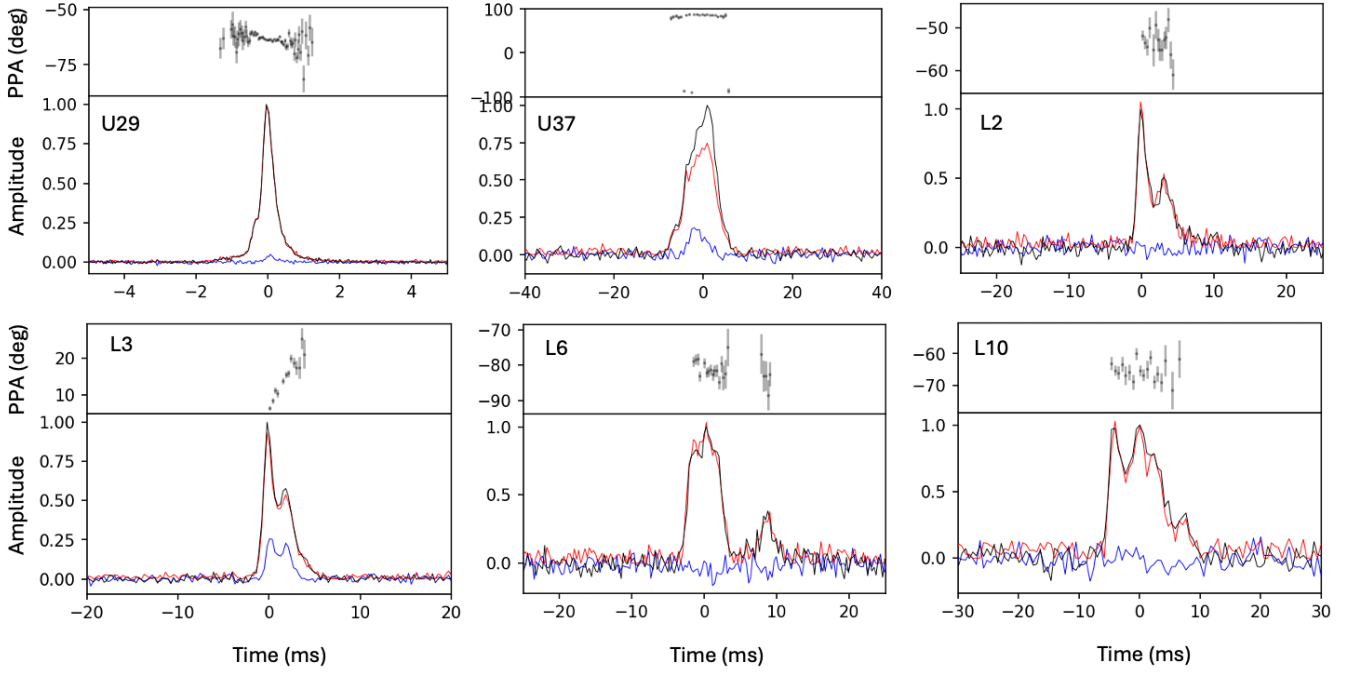


Figure 7. Polarimetric pulse profiles of a selection of bursts detected from the FRB 20240114A source. In each panel, the top shows the PPA, and the bottom shows the frequency averaged pulse profile for total intensity (I , black), linear polarisation (L , red) and circular polarisation (V , blue). The polarisation data are Faraday corrected to the RM value determined in Section 3.6.

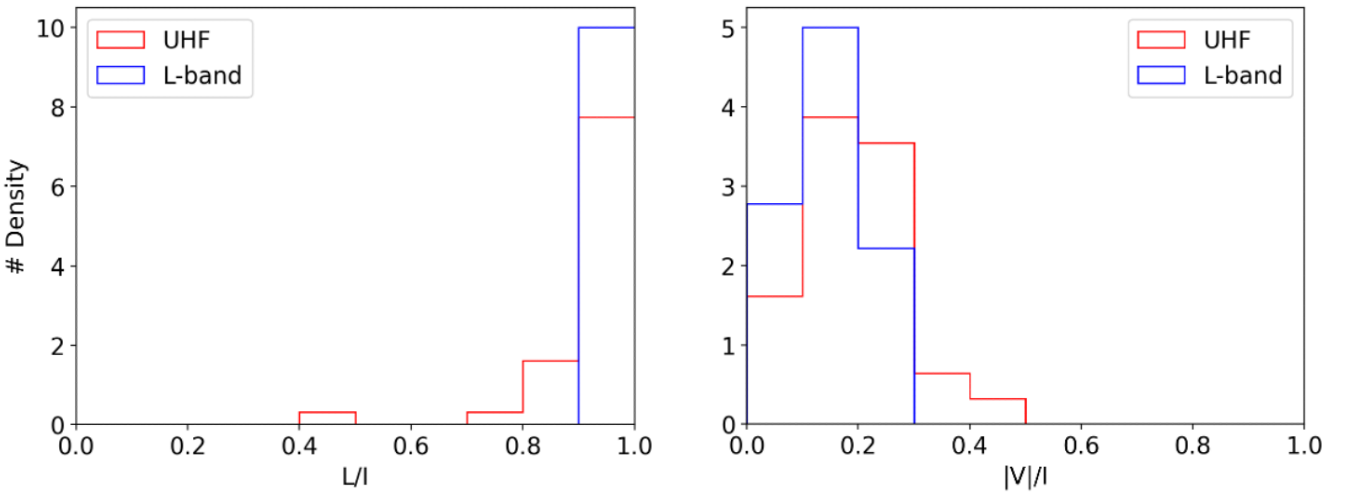


Figure 8. Distribution of linear (left) and absolute value circular (right) polarisation of the MeerKAT-detected repeat bursts from FRB 20240114A.

Depolarisation towards lower frequency has been observed in several repeating FRBs and considered to be caused by multipath propagation in the inhomogeneous magneto-ionic environment (Feng et al. 2022b). We do not observe this phenomenon in FRB 20240114A, which might suggest a different environment. Given the depolarisation has been observed to occur at different frequencies for different FRBs from < 200 MHz to > 1 GHz, it is possible the depolarisation frequency of FRB 20240114A is below our observing band. In that case, we would expect a small RM scatter based on the relation between the depolarisation and RM scattering

(O’Sullivan et al. 2012), and therefore a less turbulent, dense and/or magnetised environment for FRB 20240114A. Low-frequency observations would provide better constraints on the environment of FRB 20240114A.

4.2 Host galaxy

We can identify the host galaxy of FRB 20240114A with the arcsec localisation obtained in Section 3.2. Figure 9 shows the FRB source on top of an optical image from the DESI Legacy Survey DR10

(Dey et al. 2019), with the size of the white circle reflecting the uncertainty on the source position. This allows us to confidently associate FRB 20240114A with J212739.84+041945.8, a galaxy cataloged in the Sloan Digital Sky Survey (SDSS; Alam et al. 2015) and with an absolute r-band magnitude of -17.46 ± 0.01 AB (Bhardwaj et al. 2024). Using the Probabilistic Association of Transients to their Hosts (PATH; Aggarwal et al. 2021a) software, we found the association probability with this galaxy to be 0.997, assuming the prior on an unseen host of 0.2. This association was later independently confirmed by the EVN-PRECISE team, who localised the FRB source to the same SDSS galaxy with a conservative ~ 200 milliarcsecond precision (Snelders et al. 2024). We therefore assign J212739.84+041945.8 as the host of FRB 20240114A.

Follow-up observations of the FRB host galaxy with the Optical System for Imaging and low-Intermediate-Resolution Integrated Spectroscopy (OSIRIS) spectrograph at the Gran Telescopio Canarias (GTC) telescope detected various emission lines, leading to a redshift measurement of $z = 0.1300 \pm 0.0002$ (Bhardwaj et al. 2024), consistent with the photometric redshift of $z = 0.269 \pm 0.139$ reported in the DESI Legacy survey (Duncan 2022). In addition, the FRB host may be a dwarf star-forming galaxy (Bhardwaj et al. 2024), similar to the hosts of two active repeating sources, FRB 20121102A and FRB 20190520B (Chatterjee et al. 2017; Niu et al. 2022), which might hint at a potential persistent radio source (PRS) associated with FRB 20240114A. Note that FRB 20240114A has a much lower absolute RM than FRB 20121102A ($1.3 \times 10^5 \text{ rad m}^{-2}$; Michilli et al. 2018) and FRB 20190520B ($2.4 \times 10^4 \text{ rad m}^{-2}$; Anna-Thomas et al. 2023), and might be embedded in a less magnetised environment (see Section 4.5).

4.3 Energetics

Given the spectroscopic redshift of the FRB 20240114A host above, we can estimate the isotropic equivalent spectral energy (Petroff et al. 2019)

$$E_\nu = \frac{4\pi D_L^2 F_\nu \Delta\nu}{(1+z)\nu}, \quad (5)$$

where D_L is the luminosity distance to the source, F_ν is the specific fluence, and $\Delta\nu$ is the spectral extent of the burst. For the brightest (U29) and faintest (U12) burst in our sample, we obtained a spectral energy of $\sim 1 \times 10^{30} \text{ erg Hz}^{-1}$ (with $\Delta\nu \sim 300 \text{ MHz}$) and $\sim 6 \times 10^{27} \text{ erg Hz}^{-1}$ (with $\Delta\nu \sim 100 \text{ MHz}$), respectively. The faintest burst is only one order of magnitude more energetic than the most energetic burst from the Galactic magnetar SGR 1935+2154 (CHIME/FRB Collaboration et al. 2020b; Bochenek et al. 2020). Compared to the faintest burst from the nearby FRB 20200120E in M81, it is about four orders of magnitude more energetic (Nimmo et al. 2022). Note that this energy gap could be larger if the burst has emission outside of our observing band.

4.4 Host galaxy DM contribution

The observed DM of FRB 20240114A can be separated into four components:

$$\text{DM}_{\text{obs}} = \text{DM}_{\text{MW}} + \text{DM}_{\text{MW,halo}} + \text{DM}_{\text{IGM}} + \text{DM}_{\text{host}}, \quad (6)$$

where DM_{MW} is the contribution from the Milky Way's interstellar medium, $\text{DM}_{\text{MW,halo}}$ is from the Milky Way halo, DM_{IGM} is from the intergalactic medium (IGM), and DM_{host} is from the FRB host

including its halo and any gas local to the FRB source, all in the observer's frame. We take $\text{DM}_{\text{MW}} = 50 \text{ pc cm}^{-3}$ along the FRB line of sight based on the NE2001 model (Cordes & Lazio 2002) prediction (compared with 40 pc cm^{-3} from the YMW16 model; Yao et al. 2017), and allow for a generous uncertainty of $\pm 20 \text{ pc cm}^{-3}$. For $\text{DM}_{\text{MW,halo}}$ we adopt a range between 25 pc cm^{-3} and 80 pc cm^{-3} (Prochaska & Zheng 2019; Yamasaki & Totani 2020). At low redshifts, we can approximate the DM- z relation as a linear function (Zhang 2018; Pol et al. 2019; Cordes et al. 2022)

$$\langle \text{DM}_{\text{IGM}} \rangle \approx (855 \text{ pc cm}^{-3})z \left(\frac{H_0}{67.74 \text{ km s}^{-1} \text{ kpc}^{-1}} \right) \times \left(\frac{\Omega_b}{0.0486} \right) \left(\frac{\chi}{7/8} \right) \left(\frac{f_{\text{IGM}}}{0.83} \right), \quad (7)$$

where H_0 is the Hubble constant, Ω_b is the energy density fraction of baryons, χ is the free electron number per baryon in the Universe, and f_{IGM} is the fraction of baryons in the IGM. The cosmological parameters are normalised to the standard values measured by the Planck mission (Planck Collaboration et al. 2016), and f_{IGM} is normalised to ~ 0.83 (Fukugita et al. 1998; Li et al. 2020). We can derive a range of values for DM_{IGM} assuming a log-normal distribution with parameters:

$$\sigma_{\ln \text{DM}_{\text{IGM}}} = \{\ln[1 + (\sigma_{\text{DM}_{\text{IGM}}}/\text{DM}_{\text{IGM}})^2]\}^{1/2}, \quad (8)$$

$$\mu_{\ln \text{DM}_{\text{IGM}}} = \ln \langle \text{DM}_{\text{IGM}} \rangle - \sigma_{\ln \text{DM}_{\text{IGM}}}^2/2, \quad (9)$$

where $\sigma_{\text{DM}_{\text{IGM}}} = \sqrt{\langle \text{DM}_{\text{IGM}} \rangle \times 50 \text{ pc cm}^{-3}}$ characterises the cosmic variance of the IGM density (e.g. McQuinn 2014). For $z = 0.13$ this gives $\text{DM}_{\text{IGM}} = 92_{-42}^{+78} \text{ pc cm}^{-3}$. Altogether, we found the host-galaxy DM of FRB 20240114A to be $\text{DM}_{\text{host}} = 333_{-125}^{+90} \text{ pc cm}^{-3}$. Given this substantial host DM contribution and the host possibly being classified as a dwarf star-forming galaxy (see Section 4.2), it is worth considering the potential existence of a PRS associated with FRB 20240114A.

The host DM could be smaller if the FRB sightline intersects foreground galaxy clusters. We searched for foreground galaxy clusters that could intersect the sightline of FRB 20240114A in the galaxy cluster catalogue from the DESI legacy imaging survey (Zou et al. 2021). Within 30 arcmin of the FRB location, we found two galaxy clusters in the foreground: one with a characteristic radius of $R_{500} = 0.80 \text{ Mpc}$ (defined as the radius within which the mean density is $500\times$ the critical density of the universe) and the brightest cluster galaxy (BCG) at a photometric redshift of $z = 0.088$; the other with $R_{500} = 0.86 \text{ Mpc}$ and the BCG at a spectroscopic redshift of $z = 0.091$. However, the angular separation between FRB 20240114A and these two clusters (25.6 arcmin and 11.6 arcmin, respectively) is much larger than the angular size of the clusters (7.8 arcmin and 7.4 arcmin, respectively). Therefore, we do not consider the foreground DM contribution to be a significant contribution in this case. Future surveys such as FLIMFLAM (Lee et al. 2022) may reveal more galaxies and their redshifts in the foreground of localised FRBs and allow us to better constrain the FRB host DM.

4.5 Potential PRS association

FRB 20240114A is hyperactive and has a dwarf star-forming host galaxy and a significant host DM, similar to FRB 20121102A and

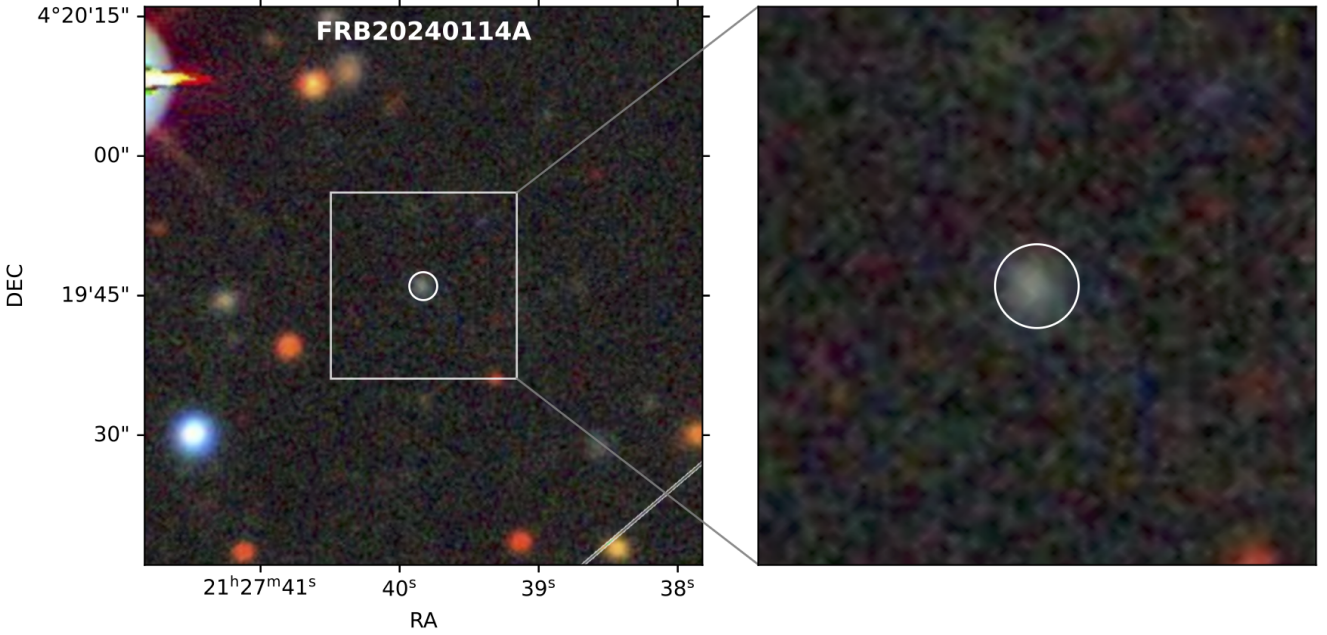


Figure 9. DESI Legacy Survey DR10 optical image in the ‘grz’ filters showing the position of the FRB 20240114A source (left) and a zoomed in view to display the association of the source with the SDSS galaxy J212739.84+041945.8 (right). The radius of the white circle reflects the uncertainty on the FRB source position.

FRB 20190520B. Meanwhile, it has an RM comparable to that observed for FRB 20201124A ($\sim 900 \text{ rad m}^{-2}$), the third FRB with a PRS detection (Bruni et al. 2023). All these could suggest the presence of a PRS associated with FRB 20240114A. Assuming that the observed RM mostly originates from the persistent emission region, we can estimate the luminosity of the PRS using a simple relation (Yang et al. 2020, 2022)

$$L_\nu \approx 5.7 \times 10^{28} \text{ erg s}^{-1} \text{ Hz}^{-1} \times \zeta_e \gamma_{\text{th}}^2 \left(\frac{|\text{RM}|}{10^4 \text{ rad m}^{-2}} \right) \left(\frac{R}{10^{-2} \text{ pc}} \right), \quad (10)$$

where ζ_e is the number density ratio between the relativistic (radiating synchrotron emission) and nonrelativistic (thermal and contributing to RM) electrons, γ_{th} is the typical Lorentz factor of the thermal electrons, and R is the size of the persistent emission region. R can be constrained to $\sim c\Delta t_{\text{per}} \approx 10^{-2} \text{ pc}$, where $t_{\text{per}} \sim 10 \text{ day}$ is the variability timescale of the PRS. $\zeta_e \gamma_{\text{th}}^2$ is constrained by the observed PRS luminosities of FRBs 20121102A, 20190520B and 20201124A to $\sim 0.1\text{--}10$ (Bruni et al. 2023).

In order to estimate the RM contribution from the FRB local environment, we can decompose the observed RM into individual components

$$\text{RM}_{\text{obs}} = \text{RM}_{\text{ion}} + \text{RM}_{\text{MW}} + \text{RM}_{\text{MW,halo}} + \text{RM}_{\text{IGM}} + \text{RM}_{\text{host}}, \quad (11)$$

where RM_{ion} is the ionospheric contribution from the Earth’s atmosphere, and the other components are the same as defined in Eq. 6, all in the observer’s frame. Given that $\text{RM}_{\text{ion}} (\sim \pm 1 \text{ rad m}^{-2}$; Sobey et al. 2019) is expected to be small, we ignore this term in Eq. 11. We also ignore RM_{IGM} as the magnetic field along the line of sight in the IGM is fairly weak ($< 21 \text{ nG}$; Ravi et al. 2016) and could undergo multiple field reversals. The Galactic RM contribu-

tion (i.e. $\text{RM}_{\text{MW}} + \text{RM}_{\text{MW,halo}}$) can be estimated using an all-sky interpolated map of the foreground MW RM contribution, which is constructed with RM measurements of radio galaxies and has a pixel scale of $\sim 1.3 \times 10^{-2} \text{ deg}^2$ (Hutschenreuter et al. 2022). Towards FRB 20240114A, $\text{RM}_{\text{MW}} + \text{RM}_{\text{MW,halo}} = -14 \pm 10 \text{ rad m}^{-2}$. Therefore, the redshift corrected host RM is $449 \pm 13 \text{ rad m}^{-2}$. This consists of RM contributions from the FRB host galaxy and local environment. As we do not have information to distinguish between these two parts, we adopt a conservative estimate of $0 \pm 10 \text{ rad m}^{-2}$ for the FRB host based on the extragalactic RM distribution of polarised radio galaxies (Vernstrom et al. 2019; Carretti et al. 2022). Taking into account the above considerations, we arrived at an RM contribution from the FRB local environment of $449 \pm 23 \text{ rad m}^{-2}$. Using this value in Eq. 10 we obtain a PRS luminosity of $\approx [0.25\text{--}25] \times 10^{27} \text{ erg s}^{-1} \text{ Hz}^{-1}$, corresponding to a flux density of $\approx [0.6\text{--}60] \mu\text{Jy}$ at the luminosity distance of FRB 20240114A. Searching for such a faint PRS would require deep continuum observations, e.g. on an integration time of $\sim \text{hr}$ with the MeerKAT L-band, and will be undertaken in a future study.

At the time of writing this manuscript, there has been a suggestion of a radio continuum counterpart associated with FRB 20240114A (Zhang & Yu 2024). We are also conducting a study of the imaging data obtained as part of this DDT and the results will be part of a separate paper. However, given the best resolution that MeerKAT can achieve is a few arcseconds, we still need VLBI follow-up to confirm the compact nature of any potential PRS.

5 CONCLUSIONS

In this paper, we report the observations of FRB 20240114A with MeerKAT, and the detection of 62 bursts in 2 hr of exposure, in-

cluding 44 in the UHF and 18 in the L-band. This confirms the high activity of the FRB 20240114 source since its discovery by CHIME/FRB. With the voltage buffer data triggered by the brightest bursts in the L-band, we make the first arcsecond localisation of the FRB source, facilitating further follow-up observations with other telescopes. This also enables us to establish a robust host galaxy association.

We find the repeat bursts of FRB 20240114A are band limited with a bandwidth of $\sim 210\text{--}270\text{ MHz}$ ($\sim 30\%\text{--}40\%$) and show frequency downward drift with a drift rate between ~ -0.1 and $\sim -34\text{ MHz ms}^{-1}$, similar to other repeating FRB sources. The fluences of the bursts we detected at UHF range from 0.12 Jy ms to 7.02 Jy ms and follow a power-law distribution with an index of $\gamma = -1.8 \pm 0.2$ above the 1 Jy ms fluence completeness limit. The overall burst rate (including all the bursts we detected) is 44 hr^{-1} and 18 hr^{-1} at UHF and L-band, respectively. We find the bursts detected in the 1 hr UHF observation approximately follow the Poissonian repetition with a constant rate $\lambda \sim 1/81\text{ s}^{-1}$ though long-term monitoring is needed to reveal any clustering behavior.

We also investigate the polarisation properties of FRB 20240114A using the triggered voltage buffer data. We find most of the bursts are $\sim 100\%$ linearly polarised and up to $\sim 20\%$ circularly polarised. The measured PPAs show a diversity of variations across the bursts, similar to that observed in bursts detected from FRB 20180301A, suggesting a magnetospheric origin of the FRB emission (Luo et al. 2020).

We identify the host galaxy of FRB 20240114A to be SDSS J212739.84+041945.8, which has a spectroscopic redshift of $z = 0.1300 \pm 0.0002$. At such redshift, the spectral energy of the bursts is estimated to be in the range of $\sim 6 \times 10^{27}\text{ erg Hz}^{-1} - 1 \times 10^{30}\text{ erg Hz}^{-1}$, and the DM contributed by the host galaxy is $333_{-125}^{+90}\text{ pc cm}^{-3}$. Assuming there exists a PRS associated with FRB 20240114A, we predict its flux density to be $\approx [0.6\text{--}60]\text{ }\mu\text{Jy}$ based on the simple relation between the luminosity of the PRS and the RM (Yang et al. 2020, 2022). We encourage deep continuum observations to search for any potential PRS.

ACKNOWLEDGEMENTS

JT would like to thank P. Weltevrede for help with the PSRSALSA software. The authors would like to thank the Director and the operators of MeerKAT and the South African Radio Astronomy Observatory (SARAO) for the prompt scheduling of the observation. This project has received funding from the European Research Council (ERC) under the European Union’s Horizon 2020 research and innovation programme (grant agreement No. 694745). JT and BWS acknowledge funding from an STFC Consolidated grant. IPM acknowledges funding from an NWO Rubicon Fellowship, project number 019.221EN.019. MC acknowledges support of an Australian Research Council Discovery Early Career Research Award (project number DE220100819) funded by the Australian Government. Parts of this research were conducted by the Australian Research Council Centre of Excellence for Gravitational Wave Discovery (OzGrav), project number CE170100004. The MeerKAT telescope is operated by the South African Radio Astronomy Observatory (SARAO), which is a facility of the National Research Foundation, an agency of the Department of Science and Innovation. SARAO acknowledges the ongoing advice and calibration of GPS systems by the National Metrology Institute of South Africa (NMISA) and the time space reference systems department of the Paris Observatory. The FB-FUSE beamforming cluster was funded, installed, and operated by

the Max-Planck-Institut für Radioastronomie and the Max-Planck-Gesellschaft.

DATA AVAILABILITY

The MeerKAT data underlying this paper will be shared on reasonable request to the corresponding author.

REFERENCES

- Adámek K., Armour W., 2020, *ApJS*, **247**, 56
- Aggarwal K., Law C. J., Burke-Spolaor S., Bower G., Butler B. J., Demorest P., Linford J., Lazio T. J. W., 2020, *Research Notes of the American Astronomical Society*, **4**, 94
- Aggarwal K., Budavári T., Deller A. T., Eftekhari T., James C. W., Prochaska J. X., Tendulkar S. P., 2021a, *ApJ*, **911**, 95
- Aggarwal K., Aggarwal D., Lewis E. F., Anna-Thomas R., Tremblay J. C., Burke-Spolaor S., McLaughlin M. A., Lorimer D. R., 2021b, *ApJ*, **922**, 115
- Alam S., et al., 2015, *ApJS*, **219**, 12
- Anna-Thomas R., et al., 2023, *Science*, **380**, 599
- Armour W., et al., 2012, in Ballester P., Egret D., Lorente N. P. F., eds, *Astronomical Society of the Pacific Conference Series Vol. 461, Astronomical Data Analysis Software and Systems XXI*. p. 33 (arXiv:1111.6399), doi:10.48550/arXiv.1111.6399
- Barr E. D., 2018, in Weltevrede P., Perera B. B. P., Preston L. L., Sanidas S., eds, *IAU Symposium Vol. 337, Pulsar Astrophysics the Next Fifty Years*. pp 175–178, doi:10.1017/S1743921317009036
- Beniamini P., Wadiasingh Z., Metzger B. D., 2020, *MNRAS*, **496**, 3390
- Bezuidenhout M. C., et al., 2022, *MNRAS*, **512**, 1483
- Bhardwaj M., Kirichenko A., Gil de Paz A., 2024, *The Astronomer’s Telegram*, **16613**, 1
- Bilous A. V., van Leeuwen J., Maan Y., Pastor-Marazuela I., Oostrum L. C., Rajwade K. M., Wang Y. Y., 2024, arXiv e-prints, p. arXiv:2407.05366
- Bochenek C. D., Ravi V., Belov K. V., Hallinan G., Kocz J., Kulkarni S. R., McKenna D. L., 2020, *Nature*, **587**, 59
- Bruni G., et al., 2023, arXiv e-prints, p. arXiv:2312.15296
- CHIME Collaboration et al., 2022, *ApJS*, **261**, 29
- CHIME/FRB Collaboration et al., 2018, *ApJ*, **863**, 48
- CHIME/FRB Collaboration et al., 2019a, *Nature*, **566**, 235
- CHIME/FRB Collaboration et al., 2019b, *ApJ*, **885**, L24
- CHIME/FRB Collaboration et al., 2020a, *Nature*, **582**, 351
- CHIME/FRB Collaboration et al., 2020b, *Nature*, **587**, 54
- CHIME/FRB Collaboration Andersen B. C., et al., 2022, *Nature*, **607**, 256
- CHIME/FRB Collaboration et al., 2023, *ApJ*, **947**, 83
- Caleb M., et al., 2020, *MNRAS*, **496**, 4565
- Caleb M., et al., 2022, *Nature Astronomy*, **6**, 828
- Caleb M., et al., 2023, *MNRAS*, **524**, 2064
- Carretti E., et al., 2022, *MNRAS*, **512**, 945
- Chatterjee S., et al., 2017, *Nature*, **541**, 58
- Chen W., Barr E., Karuppusamy R., Kramer M., Stappers B., 2021, *Journal of Astronomical Instrumentation*, **10**, 2150013
- Cho H., et al., 2020, *ApJ*, **891**, L38
- Cordes J. M., Chatterjee S., 2019, *ARA&A*, **57**, 417
- Cordes J. M., Lazio T. J. W., 2002, arXiv e-prints, pp astro-ph/0207156
- Cordes J. M., Ocker S. K., Chatterjee S., 2022, *ApJ*, **931**, 88
- Cruces M., et al., 2021, *MNRAS*, **500**, 448
- De K., Gupta Y., Sharma P., 2016, *ApJ*, **833**, L10
- Dewey R. J., Taylor J. H., Weisberg J. M., Stokes G. H., 1985, *ApJ*, **294**, L25
- Dey A., et al., 2019, *AJ*, **157**, 168
- Driessen L. N., et al., 2024, *MNRAS*, **527**, 3659
- Duncan K. J., 2022, *MNRAS*, **512**, 3662
- Feng Y., Zhang Y.-K., Li D., Yang Y.-P., Wang P., Niu C.-H., Dai S., Yao J.-M., 2022a, *Science Bulletin*, **67**, 2398

- Feng Y., et al., 2022b, *Science*, 375, 1266
- Fonseca E., et al., 2020, *ApJ*, 891, L6
- Fukugita M., Hogan C. J., Peebles P. J. E., 1998, *ApJ*, 503, 518
- Gaensler B. M., Madsen G. J., Chatterjee S., Mao S. A., 2008, *Publ. Astron. Soc. Australia*, 25, 184
- Geyer M., et al., 2021, *MNRAS*, 505, 4468
- Gordon A. C., et al., 2023, *ApJ*, 954, 80
- Gourdji K., Michilli D., Spitler L. G., Hessels J. W. T., Seymour A., Cordes J. M., Chatterjee S., 2019, *ApJ*, 877, L19
- Hessels J. W. T., et al., 2019, *ApJ*, 876, L23
- Hilmarsson G. H., Spitler L. G., Main R. A., Li D. Z., 2021, *MNRAS*, 508, 5354
- Hotan A. W., van Straten W., Manchester R. N., 2004, *Publ. Astron. Soc. Australia*, 21, 302
- Hutschenreuter S., et al., 2022, *A&A*, 657, A43
- Ioka K., Zhang B., 2020, *ApJ*, 893, L26
- Jankowski F., et al., 2023, *MNRAS*, 524, 4275
- Jiang J.-C., et al., 2022, *Research in Astronomy and Astrophysics*, 22, 124003
- Kirsten F., et al., 2022, *Nature*, 602, 585
- Kramer M., Liu K., Desvignes G., Karuppusamy R., Stappers B. W., 2024, *Nature Astronomy*, 8, 230
- Kumar P., Shannon R. M., Lower M. E., Bhandari S., Deller A. T., Flynn C., Keane E. F., 2022, *MNRAS*, 512, 3400
- Kumar A., Maan Y., Bhusare Y., 2024, *The Astronomer's Telegram*, 16452, 1
- Lanman A. E., et al., 2022, *ApJ*, 927, 59
- Lee K.-G., Ata M., Khrykin I. S., Huang Y., Prochaska J. X., Cooke J., Zhang J., Batten A., 2022, *ApJ*, 928, 9
- Levin Y., Beloborodov A. M., Bransgrove A., 2020, *ApJ*, 895, L30
- Li Z., Gao H., Wei J. J., Yang Y. P., Zhang B., Zhu Z. H., 2020, *MNRAS*, 496, L28
- Li D., et al., 2021, *Nature*, 598, 267
- Luo R., et al., 2020, *Nature*, 586, 693
- Majid W. A., et al., 2021, *ApJ*, 919, L6
- Marcote B., et al., 2020, *Nature*, 577, 190
- Marthi V. R., et al., 2021, *MNRAS*, 505, 4468
- Mauch T., et al., 2020, *ApJ*, 888, 61
- McConnell D., et al., 2020, *Publ. Astron. Soc. Australia*, 37, e048
- McQuinn M., 2014, *ApJ*, 780, L33
- McKinnon R., et al., 2023, *ApJ*, 951, 82
- Michilli D., et al., 2018, *Nature*, 553, 182
- Mitra D., Arjunwadkar M., Rankin J. M., 2015, *ApJ*, 806, 236
- Nimmo K., et al., 2021, *Nature Astronomy*, 5, 594
- Nimmo K., et al., 2022, *Nature Astronomy*, 6, 393
- Niu C. H., et al., 2022, *Nature*, 606, 873
- O'Sullivan S. P., et al., 2012, *MNRAS*, 421, 3300
- Offringa A. R., Smirnov O., 2017, *MNRAS*, 471, 301
- Offringa A. R., et al., 2014, *MNRAS*, 444, 606
- Oppermann N., Yu H.-R., Pen U.-L., 2018, *MNRAS*, 475, 5109
- Panda U., Bhattacharyya S., Dudeja C., Kudale S., Roy J., 2024, *The Astronomer's Telegram*, 16494, 1
- Pandhi A., et al., 2024, *arXiv e-prints*, p. arXiv:2401.17378
- Pastor-Marazuela I., et al., 2021, *Nature*, 596, 505
- Pastor-Marazuela I., et al., 2023, *A&A*, 678, A149
- Petroff E., et al., 2016, *Publ. Astron. Soc. Australia*, 33, e045
- Petroff E., Hessels J. W. T., Lorimer D. R., 2019, *A&ARv*, 27, 4
- Planck Collaboration et al., 2016, *A&A*, 594, A13
- Platts E., et al., 2021, *MNRAS*, 505, 3041
- Pleunis Z., et al., 2021, *ApJ*, 923, 1
- Pol N., Lam M. T., McLaughlin M. A., Lazio T. J. W., Cordes J. M., 2019, *ApJ*, 886, 135
- Price D. C., Flynn C., Deller A., 2021, *Publ. Astron. Soc. Australia*, 38, e038
- Prochaska J. X., Zheng Y., 2019, *MNRAS*, 485, 648
- Rajwade K. M., et al., 2020, *MNRAS*, 495, 3551
- Rajwade K. M., et al., 2022, *MNRAS*, 514, 1961
- Rajwade K. M., et al., 2024, *MNRAS*, 532, 3881
- Ravi V., et al., 2016, *Science*, 354, 1249
- Ravi V., et al., 2022, *MNRAS*, 513, 982
- Sanidas S., Caleb M., Driessen L., Morello V., Rajwade K., Stappers B. W., 2018, in Weltevrede P., Perera B. B. P., Preston L. L., Sanidas S., eds, *IAU Symposium Vol. 337, Pulsar Astrophysics the Next Fifty Years*. pp 406–407, doi:10.1017/S1743921317009310
- Seymour A., Michilli D., Pleunis Z., 2019, *DM_phase: Algorithm for correcting dispersion of radio signals*, *Astrophysics Source Code Library*, record ascl:1910.004
- Shannon R. M., et al., 2018, *Nature*, 562, 386
- Shin K., CHIME/FRB Collaboration 2024, *The Astronomer's Telegram*, 16420, 1
- Snelders M. P., et al., 2024, *The Astronomer's Telegram*, 16542, 1
- Sobey C., et al., 2019, *MNRAS*, 484, 3646
- Tendulkar S. P., et al., 2017, *ApJ*, 834, L7
- Tian J., Pastor-Marazuela I., Stappers B., Rajwade K., Caleb M., Bezuidenhout M., Barr E., Kramer M., 2024, *The Astronomer's Telegram*, 16446, 1
- Uttarkar P. A., Kumar P., Lower M. E., Shannon R. M., 2024, *The Astronomer's Telegram*, 16430, 1
- Vernstrom T., Gaensler B. M., Rudnick L., Andernach H., 2019, *ApJ*, 878, 92
- Wang W., Zhang B., Chen X., Xu R., 2019, *ApJ*, 876, L15
- Wang W.-Y., Xu R., Chen X., 2020, *ApJ*, 899, 109
- Wardle J. F. C., Kronberg P. P., 1974, *ApJ*, 194, 249
- Weltevrede P., 2016, *A&A*, 590, A109
- Xu H., et al., 2022, *Nature*, 609, 685
- Yamasaki S., Totani T., 2020, *ApJ*, 888, 105
- Yang Y.-P., Li Q.-C., Zhang B., 2020, *ApJ*, 895, 7
- Yang Y.-P., Lu W., Feng Y., Zhang B., Li D., 2022, *ApJ*, 928, L16
- Yao J. M., Manchester R. N., Wang N., 2017, *ApJ*, 835, 29
- Zhang B., 2018, *ApJ*, 867, L21
- Zhang B., 2023, *Reviews of Modern Physics*, 95, 035005
- Zhang X., Yu W., 2024, *The Astronomer's Telegram*, 16695, 1
- Zhang J., et al., 2024a, *The Astronomer's Telegram*, 16433, 1
- Zhang J., et al., 2024b, *The Astronomer's Telegram*, 16505, 1
- Zou H., et al., 2021, *ApJS*, 253, 56
- van Straten W., Bailes M., 2011, *Publ. Astron. Soc. Australia*, 28, 1

APPENDIX A: POLARISATION PROFILES

In Figure A1 we show the polarisation profiles of all the bursts we detected in the MeerKAT observation and triggered the voltage buffer dump (see Table 1). The different Stokes parameters are displayed in different colors with total intensity I being black, linear polarisation L red and circular polarisation V blue, and the PPA is displayed in the top of each panel. These polarisation data are used to calculate the linear and circular polarisation fractions for each burst, as shown in Table 1. Note that although bursts U44 and L9 have no triggered data, they are within the 300 ms voltage data triggered by the next burst (see Figure 1 for their proximity to the next burst), and thus have polarisation data. However, burst U44 is not shown here for its low S/N.

This paper has been typeset from a \LaTeX file prepared by the author.

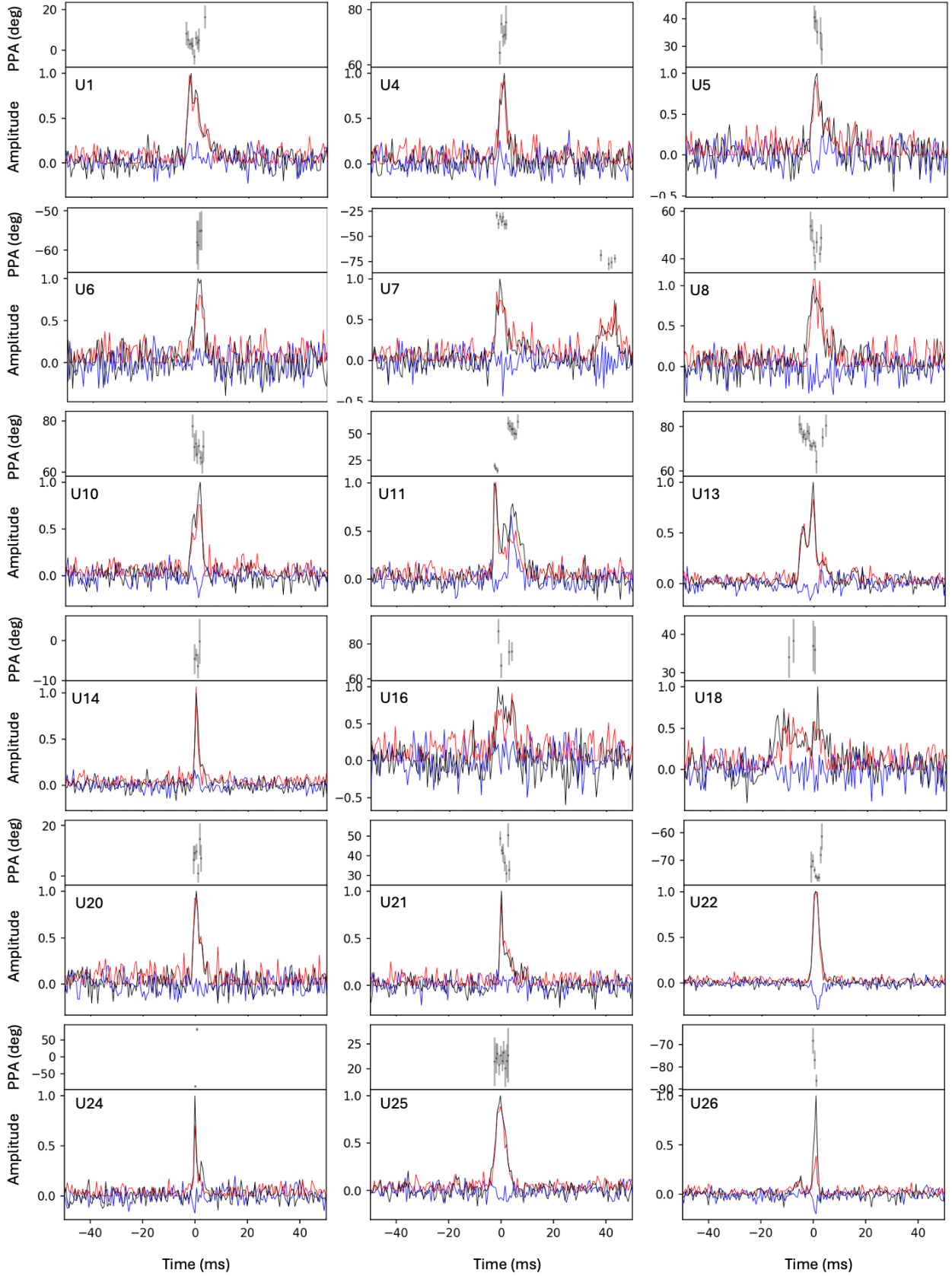


Figure A1. Polarisation profiles of all the MeerKAT-detected repeat bursts from FRB 20240114A with polarisation data. The top of each panel shows the PPA, and the bottom shows the total intensity I (black), linear polarisation L (red) and circular polarisation V (blue). These data are all coherently dedispersed to the DM value determined in Section 3.1 and derotated to the RM value in Section 3.6.

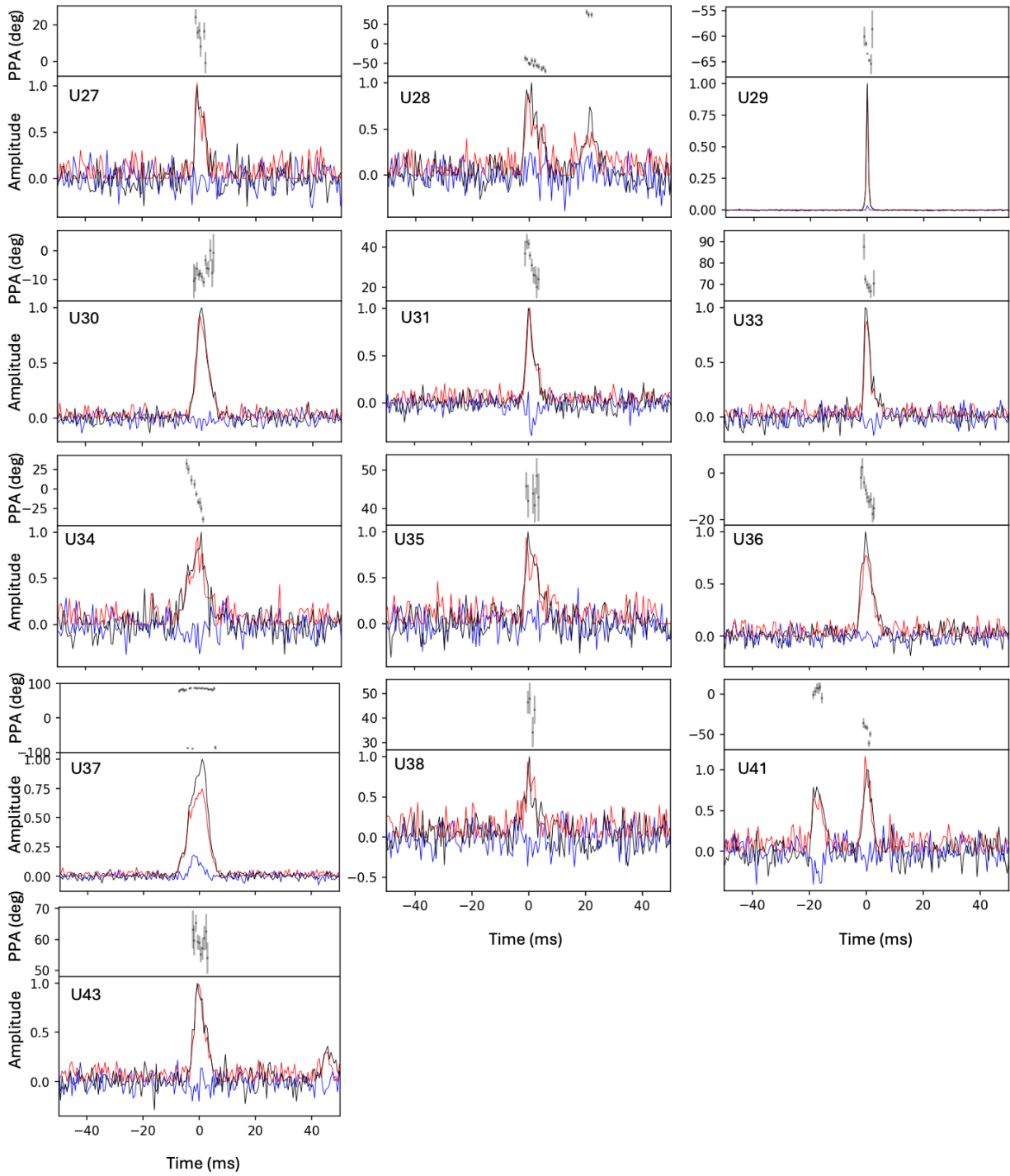


Figure A1 (Continued.).

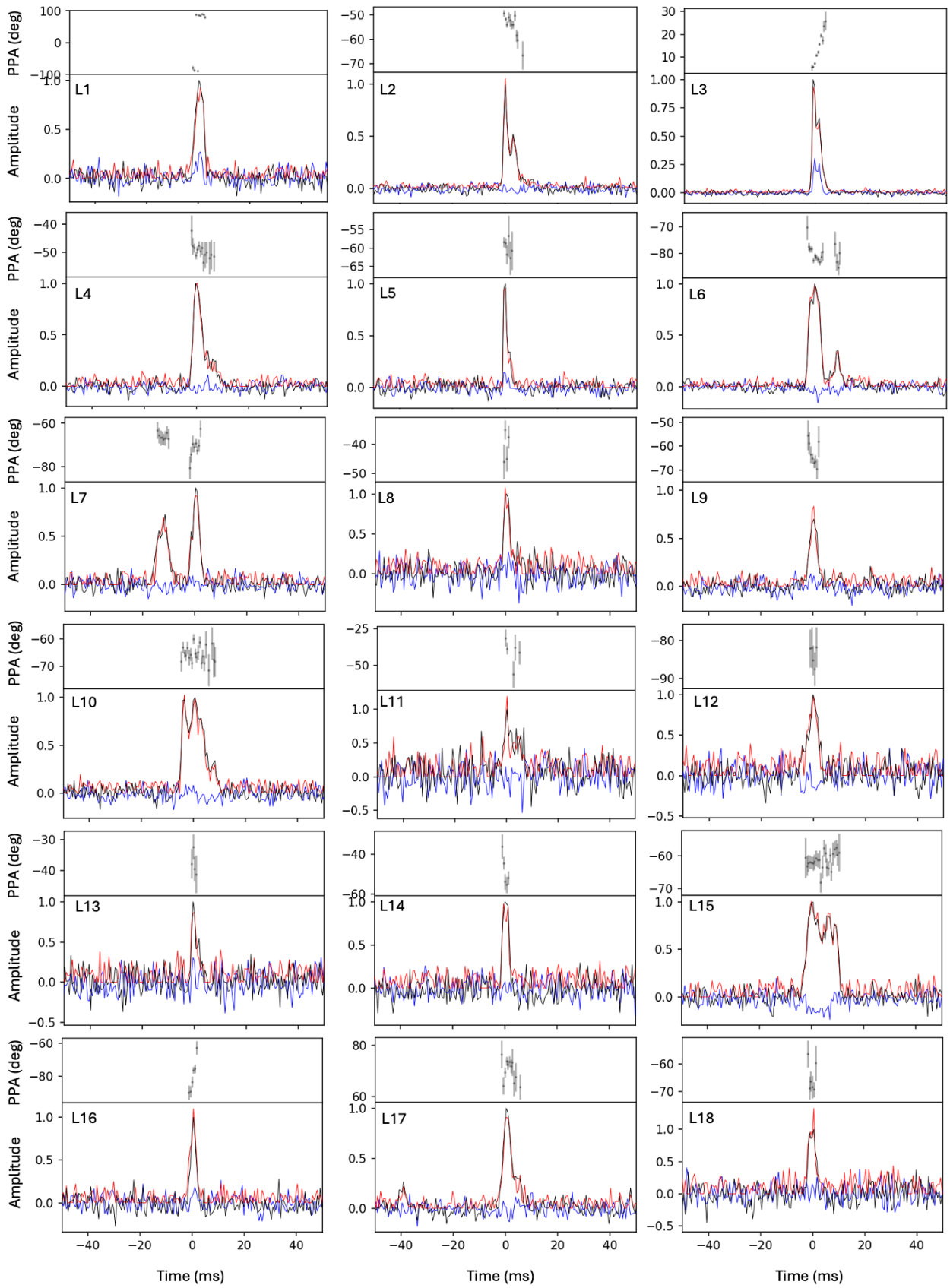


Figure A1 (Continued.).